The relationship between the plasmapause and outer belt electrons

Goldstein, J.
Funsten, Herbert O.
Reeves, Geoffrey D.

To be published in: Journal of Geophysical Research: Space Physics

DOI to publisher's version: 10.1002/2016JA023046

The Relationship Between the Plasmapause and Outer Belt Electrons

J. Goldstein[1, 2], D. N. Baker[3], J. B. Blake[4], S. De Pascuale[5], H. O. Funsten[6], A. Jaynes[3], J. Jahn[1, 2], C. Kletzing[5], W. S. Kurth[5], W. Li[7] G. D. Reeves[6], H. Spence[8]

Key points:

- Two outer belts, a dynamic zone near the plasmapause, and a stable zone deep within cold plasma
- Relativistic electron flux earthward of the peak is anticorrelated with dense plasma
- Electron lifetimes in stable outer belt are consistent with decay by plasmaspheric hiss

Abstract.

We quantify the spatial relationship between the plasmapause and outer belt electrons for a five-day period, 15–20 January 2013, by comparing locations of relativistic electron flux peaks to the plasmapause. A peak-finding algorithm is applied to 1.8–7.7 MeV relativistic electron flux data. A plasmapause gradient-finder is applied to wave-derived electron number densities >10 cm^{-3}. We identify two outer belts. Outer belt 1 is a stable zone of >

J. Goldstein, J. Jahn, Southwest Research Institute, 6220 Culebra Rd, San Antonio, TX 78228 USA (jgoldstein@swri.edu)

D. N. Baker, A. Jaynes, Laboratory for Atmospheric and Space Physics, University of Colorado, 1234 Innovation Drive, Boulder, CO 80303-7814

J. B. Blake, Mail Stop M2-259, The Aerospace Corporation, P.O. Box 92957, Los Angeles, CA 90009

C. Kletzing, W. S. Kurth, S. De Pascuale, Department of Physics and Astronomy, 203 Van Allen Hall, University of Iowa, Iowa City, Iowa, USA

W. Li, Department of Atmospheric and Oceanic Sciences, UCLA, Los Angeles, California, USA.

G. D. Reeves, H. O. Funsten, Los Alamos National Laboratory, Los Alamos, NM 87545

H. Spence, Institute for the Study of Earth, Oceans, and Space, University of New Hampshire, Morse Hall, 8 College Road, Durhan, NH 03824 USA

[1] Space Science and Engineering Division,

3 MeV electrons located 1–2 R_E inside the plasmapause. Outer belt 2 is a dynamic zone of $<$ 3 MeV electrons within 0.5 R_E of the moving plasmapause. Electron fluxes earthward of each belt's peak are anti-correlated with cold plasma density. Belt 1 decayed on hiss timescales prior to a disturbance on 17 January, and suffered only a modest dropout, perhaps owing to shielding by the plasmasphere. Afterward, the partially-depleted belt 1 continued to decay at the initial rate. Belt 2 was emptied out by strong losses during the disturbance, but restored within 24 hours. For global context we use a plasmapause test particle (PTP) simulation, from which we derive a new plasmaspheric index F_p, the fraction of a circular drift orbit inside the plasmapause. We find that the locally-measured plasmapause is (for this event) a good proxy for the globally-integrated opportunity for losses in the cold plasma. Our analysis of the 15–20 January 2013 time interval confirms that high-energy electron storage rings can persist for weeks or even months if prolonged quiet conditions prevail.

Southwest Research Institute, San Antonio, TX, USA.

[2] Department of Physics and Astronomy, University of Texas San Antonio, San Antonio, TX, USA.

[3] Laboratory for Atmospheric and Space Physics, University of Colorado, Boulder, CO, USA.

[4] The Aerospace Corporation, Los Angeles, CA USA.

[5] Department of Physics and Astronomy, University of Iowa, Iowa City, IA, USA.

[6] Los Alamos National Laboratory, Los Alamos, NM USA.

[7] Department of Atmospheric and Oceanic Sciences, UCLA, Los Angeles, California, USA.

[8] Institute for the Study of Earth, Oceans, and Space, University of New Hampshire, Durham, NH, USA.

1. Introduction

The inner magnetosphere comprises several distinct particle populations. In this paper we focus on the relationship between the coldest (plasmasphere) and the most energetic (radiation belts) populations.

The plasmasphere is a region of cold (few eV) plasma that surrounds Earth up to a few Earth radii (R_E) [*Lemaire and Gringauz*, 1998]. It is composed predominantly of H^+, with time-varying amounts of He^+ and O^+ present [*Olsen et al.*, 1987; *Horwitz et al.*, 1990; *Craven et al.*, 1997]. The plasmasphere's outer boundary, the plasmapause, is highly dynamic, moving inward (outward) in response to enhanced (diminished) geomagnetic activity. During active times the outer plasmasphere is eroded, producing plumes of cold dense plasma that extend to the dayside magnetopause in the afternoon sector [*Chappell et al.*, 1970; *Chappell*, 1974; *Goldstein and Sandel*, 2005].

The radiation belts are zones of relativistic electrons and protons encircling the Earth [*Van Allen and Frank*, 1959]. The electrons' radial structure is controlled by the dynamic imbalance between source and loss processes [*Baker et al.*, 1994; *Turner et al.*, 2014a, b; *Ukhorskiy et al.*, 2015; *Reeves et al.*, 2016]. Historically, the radial structure has consisted of a relatively stable inner belt (with electron lifetimes >100 days) and a more dynamic outer belt (lifetimes as short as a day or less). Trapped fluxes in the outer belt can vary by two orders of magnitude on timescales of a few hours to days, and the peak flux location is extremely variable. Recent observations have revealed a quite different three-belt radial structure, containing two outer belts of MeV electrons [*Baker et al.*, 2013; *Hudson et al.*, 2014] and one inner belt composed of electrons with energies < 900 keV [*Li et al.*, 2015b; *Fennell et al.*, 2015].

The plasmasphere overlaps with the outer belt(s) to a varying degree, occasionally reaching extreme overlap [*O'Brien et al.*, 2003; *Baker et al.*, 2004; *Goldstein et al.*, 2005c; *Li et al.*, 2006; *Baker et al.*, 2013; *Baker et al.*, 2014], and plasmaspheric drainage plumes cross both the outer belt and the ring current [*Goldstein et al.*, 2005b; *Borovsky et al.*, 2014]. These overlap regions may be favored locations for the growth of waves that can cause loss of outer belt electrons [*Thorne and Kennel*, 1971; *Millan and Thorne*, 2007]. One such wave is plasmaspheric whistler-mode hiss [*Thorne et al.*, 1973; *Meredith et al.*, 2004; *Bortnik et al.*, 2008; *Summers et al.*, 2014; *Spasojevic et al.*, 2015; *Li et al.*, 2015a; *Kim et al.*, 2015]. For outer belt electrons of hundreds of keV to a few MeV, the energy- and L-dependent loss timescales due to hiss can range from a few days to tens of days [*Lyons et al.*, 1972; *Lyons and Thorne*, 1973; *Goldstein et al.*, 2005c; *Ni et al.*, 2013; *Li et al.*, 2014a; *Jaynes et al.*, 2014; *Breneman et al.*, 2015; *Ma et al.*, 2015; *Hardman et al.*, 2015]. Another potentially important loss term is the growth of electromagnetic ion cyclotron (EMIC) waves [*Fraser and Nguyen*, 2001; *Fraser et al.*, 2005, 2010; *Loto'aniu et al.*, 2005; *Halford et al.*, 2010; *Denton et al.*, 2014; *Meredith et al.*, 2014; *Engebretson et al.*, 2015; *Wang et al.*, 2015; *Yu et al.*, 2015b; *Halford et al.*, 2015]. Theoretically, both EMIC wave growth and the effectiveness of EMIC-induced pitch angle scattering can be increased in regions of dense cold plasma where the resonance cutoff is lower (especially with heavy ion enrichment) [*Summers and Thorne*, 2003; *Meredith et al.*, 2003; *Clilverd et al.*, 2015; *Rodger et al.*, 2015], and strong diffusion can result in loss timescales of several hours to a day [*Meredith et al.*, 2003; *Yu et al.*, 2015a]. Observational studies have shown dynamic correlations between EMIC waves and MeV electron precipitation, especially on the duskside where plasmaspheric plumes often reside [*Lorentzen et al.*, 2000; *Millan et al.*, 2002, 2007; *Loto'aniu et al.*, 2006; *Woodger*, 2012; *Woodger et al.*, 2015; *Li et al.*, 2014b; *Blum et al.*, 2015]. On the other hand, both theoretical and observational evidence indicates that MeV electron precipitation by EMIC waves is limited to small equatorial pitch angles, so that the core MeV population may not always be affected [*Kersten et al.*, 2014; *Usanova et al.*, 2014; *Yu et al.*, 2015a].

In addition to hosting the growth of waves associated with loss terms, cold dense plasma can hinder or alter chorus waves that can scatter electrons both in pitch angle and energy (i.e., resulting in loss or energization) [*Burtis and Helliwell*, 1969; *Sazhin and Hayakawa*, 1992; *Meredith et al.*, 2001; *Horne et al.*, 2005; *Summers et al.*, 2007]. Also controlled by the high mass density inside the plasmasphere is the propagation of ultra-low-frequency (ULF) waves that can cause energization and radial transport of electrons whose drift times are comparable to the ULF periods [*Hudson et al.*, 1995; *Li et al.*, 1998; *Elkington et al.*, 2003; *Hudson et al.*, 2014]. The plasmasphere can shield electrons within it, by damping the ULF waves involved in outward radial diffusion that contributes to magnetopause shadowing [*Shprits et al.*, 2006; *Turner et al.*, 2014a].

The spatial relationship between the plasmapause and outer belt electrons has been an area of research for decades. Multiple past studies have demonstrated that the quiet-time slot region is produced by wave-particle interactions between energetic electrons and plasmaspheric hiss [*Lyons et al.*, 1972], and that the plasmasphere and outer belt are generally spatially complementary on timescales longer than a few days [*O'Brien et al.*, 2003; *Baker et al.*, 2004; *Goldstein et al.*, 2005c]. For example, *Li et al.* [2006]

analyzed a decade of low-altitude >2 MeV electron data and found that the outer extent of the slot region lined up with the plasmapause location (as determined by an empirical model). The very earliest observations by the Van Allen Probes mission launched in 2012 [*Reeves*, 2007; *Mauk et al.*, 2013] showed something new, however: two outer belts, with clear evidence of a long-timescale overlap between the plasmasphere and both outer belts [*Baker et al.*, 2013; *Hudson et al.*, 2014]. These apparently contradictory results raise the question: what is the relationship between the plasmapause and the outer belt electrons? The plasmapause and outer belts represent a fundamentally complex system that spans large spatial, temporal and spectral scales. Understanding associations between their structure and dynamics provides insight into the underlying physics and drivers. With few exceptions [e.g., *Goldstein et al.*, 2005c; *Johnston and Anderson*, 2010; *Baker et al.*, 2014] previous studies have addressed this important question using plasmapause locations from models rather than observations. Still needed is a systematic comparison of observed plasmapause and outer belt locations that incorporates the two-outer-belt configuration.

In this paper we take the first step using data from two Van Allen Probes instruments from the five-day interval 15–20 January 2013. To determine the plasmapause we use electron number densities, derived from plasma wave data obtained by the Electric and Magnetic Field Instrument Suite and Integrated Science (EMFISIS) suite [*Kletzing et al.*, 2013]. To characterize the relativistic electrons we use data from the Relativistic Electron-Proton Telescope (REPT) instrument [*Baker et al.*, 2013]. A plasmapause test particle (PTP) simulation [*Goldstein et al.*, 2005a, 2014a, b] provides global context for the local EMFISIS-derived densities. Section 2 describes the automated peak/edge and plasma-pause extractions. Section 3 quantifies the spatial relationship between the plasmapause and outer belts. Section 4 analyzes the PTP model results. In Section 5 we interpret our results, with a major focus on plasmaspheric hiss. Our summary is found in Section 6.

2. Peak/Edge and Plasmapause Extractions

In this section we give an overview of the 15–20 January 2013 event, and describe our automated methods to extract from Van Allen Probes data the maxima (and their associated inner edges) of the relativistic outer-belt electron flux, as well as the plasmapause locations.

2.1. Event: 15–20 January 2013

Figure 1 shows an overview of the five-day interval 15–20 January 2013, during which time there was a moderate geomagnetic storm ($\mathrm{Dst}_{\mathrm{min}} \sim -50$ nT) that commenced at 1330 UT on 17 January. Figure 1a shows two solar wind parameters and two cardinal magnetospheric boundaries. The solar wind electric (E) field is computed as $E_{\mathrm{SW}} \equiv V_{\mathrm{SW}} B_{\mathrm{Z}}$ from 5 min OMNI data in GSE coordinates, derived from upstream measurements made by the Wind [*Ogilvie et al.*, 1995; *Lepping et al.*, 1995] and Advanced Composition Explorer (ACE) missions [*Stone et al.*, 1998]. Negative E_{SW} is defined to correspond to times when the interplanetary magnetic field (IMF) is southward. The solar wind pressure (P_{SW}) is shown in purple. The subsolar magnetopause location (R_{MP}) is computed from the model of *Shue et al.* [1997]. The green curve shows the minimum plasmapause location obtained from the test particle simulation that is described in Section 4. The minimum plasmapause, defined at a given time as the minimum boundary location for that instant's 2D equatorial plasmapause shape, provides a time-varying index of the most intense erosion.

Between 0830 UT and 1330 UT (17 January) the solar wind pressure increased fourfold to nearly 17 nPa, compressing the model subsolar magnetopause past geostationary orbit to a minimum value of 6.2 R_E at 1340 UT. At 1330 UT on 17 January (the solid vertical line) the IMF rotated to a sustained southward direction, initiating over 10 h of erosion, in which the minimum plasmapause dipped to $L < 3$. (The two dashed vertical lines indicate times selected for examples of our peak-finding analysis in Section 2.2.)

Figure 1b and Figure 1c show electron flux spectrograms for two energies, measured by the Relativistic Electron-Proton Telescope (REPT) on Van Allen Probes A. The data are binned in time and space as follows. There is one time bin per half-orbit (perigee to apogee or vice versa), and there are 61 bins spanning $L^* = 1$ to 7 (i.e., the radial resolution is $0.1L^*$). Binned fluxes are spin-averaged, and values of L^* were calculated using the (static) OP77 model [*Olson and Pfitzer*, 1977]. Note that the signal below $L^* \approx 2.5$ (in both spectrograms) represents a known proton background in the electron channels, rather than real electron measurements. It has been shown that the inner zone is devoid of measurable electrons in the REPT energy range during the Van Allen Probes era [*Li et al.*, 2015b; *Fennell et al.*, 2015]

The REPT A spectrogram data depict a strongly energy-dependent response to the disturbance of 1330 UT on 17 January. The disturbance (black solid line) caused a depletion of 1.8 MeV outer belt electrons (Figure 1c), across a range of L^*. Farther out ($L^* > 4$) the 1.8 MeV flux dropped by 1 to 2 orders of magnitude. At smaller L^* for both 1.8 MeV and 4.2 MeV (Figure 1b) the flux decreased by a more modest factor of 2 to 3. The higher-L^* ($L^* > 4$) dropout occurred earlier than at lower L^*. Main phase dropouts are thought to be caused by a combination of processes including magnetopause shadowing and outward radial transport (at large L^*) and the adiabatic effect (at small L^*) [*Turner et al.*, 2014a; *Ukhorskiy et al.*, 2015], as well as by EMIC waves [*Drozdov et al.*, 2015]. This disturbance-time flux decrease is discussed further in Section 5.

The morphology of the 1.8 MeV outer belt region changed as a result of the 17 January disturbance: beforehand there were two outer belts of 1.8 MeV electrons, and afterward there was one outer belt. During the 1.5 days prior to the 17 January disturbance, outer belt 1 peaked at $L^* \approx 4$ and outer belt 2 peaked at $L^* \approx 5.5$ (Figure 1c). In the 12 hours directly before the disturbance hit, while solar wind pressure was elevated and the IMF was northward (Figure 1a), the two outer belts moved inward; outer belt 1 by $\sim 0.5L^*$ and outer belt 2 by $\sim 0.8L^*$. After the disturbance, what remained of outer belt 1 decayed and outer belt 2 was restored.

The above change in outer belt morphology did not occur for 4.2 MeV and higher: both before and after the disturbance the 4.2 MeV electrons occupied a single outer belt at $L^* \approx 3.5$ (Figure 1b). Thus outer belt 1 may be interpreted as a "storage ring" [*Baker et al.*, 2013] of high-energy electrons that persisted (with a modest drop) through the disturbance while the higher-L^* outer belt 2 experienced large dynamical changes. For energies ≥ 4.2 MeV this stable storage ring was the dominant flux feature during the 15–20 January 2013 event.

In the next section we detail our method for extracting peaks and edges from the relativistic electron data.

2.2. Electron Peak and Edge Finder

For this study we use an automated algorithm to extract the locations of peaks and edges from the REPT spectrogram data. First, each flux versus L^* profile at $0.1L^*$ resolution is smoothed with an 8-point boxcar average, which is sufficient to smooth spatial and temporal L^* variations occurring over small scales and to retain and identify systematic flux variations occurring at scales greater than $\sim 0.5L^*$. In each boxcar-smoothed profile $f(L^*)$, the algorithm identifies peaks (f_{peak}) via two differential criteria: $d \log f/dL^* \approx 0$ and $d^2 \log f/dL^{*2} < 0$. For each peak f_{peak} thus identified, the corresponding edge is where $f_{\text{edge}} = f_{\text{peak}} \exp(-1)$ for L^* values smaller than the peak. Figure 2 shows the result of applying this peak and edge finder to REPT data at two selected times before and after the disturbance: 0048 UT on 17 January (Figure 2a) and 2139 UT on 18 January (Figure 2b). These two times are indicated in Figure 1 by vertical dashed lines. At each time the algorithm was applied to eight REPT energy channels: $[1.8, 2.1, 2.6, 3.4, 4.2, 5.2, 6.3, 7.7]$ MeV.

In Figure 2 the peak locations (L_{peak}) of outer belts 1 and 2 are indicated by numbered ("1" or "2") dots and vertical lines. The point at $L^* < 2.5$ labeled "p^+" also satisfies the two differential f_{peak} critera above, but this peak is rejected because it results from the proton background signal, as noted earlier. For each peak the corresponding edge location L_{edge} is indicated by the nearest dashed line inward of the peak.

2.3. Plasmapause Finder

To locate the plasmapause for this study we use number density data derived from plasma waves measured by the Electric and Magnetic Field Instrument Suite and Integrated Science (EMFISIS) suite on Van Allen Probes A. The extraction of electron number densities (n_e) from the 15–20 January 2013 EMFISIS wave data is briefly discussed in Appendix A1 and described in detail in *Goldstein et al.* [2014b]. Figure 3 shows two example density profiles, from 0138–0610 UT on 15 January and 1926–2354 UT on 18 January. These profiles have been interpolated to the L^* bins used for the REPT spectrograms, yielding an EMFISIS n_e spectrogram (cf. Figure 4b). To extract plasmapause locations from profiles like these, we use an automated algorithm. First, each density versus L^* profile is smoothed with a 4-point boxcar average. In each smoothed profile $n(L^*)$ the algorithm identifies the plasmapause (L_P) as the outermost location satisfying two criteria: $d\log n/dL^* < 0$ and $n_e \geq 10\,\mathrm{cm}^{-3}$. That is, the plasmapause is found as the outermost negative density gradient crossing the threshold value $10\,\mathrm{cm}^{-3}$, where the threshold is applied to the unsmoothed data. Where the sampled outermost gradient does not cross the threshold, the minimum extracted density (outermost L^* value) is used. Plumes and other subglobal structure, that might otherwise complicate the automated plasmapause detection, are not a major concern in the predawn MLT sector where these data were taken.

2.4. Extractions for 15–20 January 2013

The automated algorithms were applied to the binned Van Allen Probes A REPT and EMFISIS data from 15–20 January 2013. Figure 4a shows the 1.8 MeV REPT A spectrogram, with extracted peak locations (L_peak, solid lines) and edges (L_edge, dashed lines). Outer belt 1 (i.e., the storage ring) is plotted in blue, and outer belt 2 is in black. Figure 4b contains a 2D spectrogram of EMFISIS A number density (n_e), binned in L^* and time to match the REPT A spectrogram's resolution and cadence. The extracted plasmapause (L_P) is the black line.

On 15 and 16 January the 1.8 MeV outer belts 1 and 2 were relatively stable, with average peak locations of L^* =3.9 (outer belt 1) and L^* =5.5 (outer belt 2). Starting on 17 January both outer belts moved inward; by the time of the disturbance (1330 UT on 17 January), outer belts 1 and 2 had migrated to L^* =3.4 ($\Delta L^* = -0.5$) and $L^* = 4.7$

($\Delta L^* = -0.8$), respectively. As a result of the disturbance, outer belt 2 experienced a strong dropout in which flux decreased by a factor of > 100 (cf. arrow labeled 'dropout'); for this half-orbit bin the automated algorithm identified no peak for belt 2. After the dropout outer belt 2 recovered, and late on day 18 stabilized to a mean value of $L^* = 4.6$. Outer belt 1 experienced a modest (factor of 2) decrease in flux from the disturbance, but then decayed (rather than recovering) so that by about 1700 UT, for $L^* < 3.4$ there was no 1.8 MeV peak, only a plateau in flux.

The plasmapause varied somewhat prior to the disturbance. Given the relatively quiet conditions that prevailed (Kp≤ 2), and judging from the simulated plasmasphere [*Goldstein et al.*, 2014b], this early variability in the EMFISIS-measured plasmapause was produced by the rotation of quiet-time local-time structure past the Van Allen Probes A spacecraft. The 17 January disturbance caused a global plasmaspheric erosion (cf. Figure 1a and *Goldstein et al.* [2014b]), which appears in the binned EMFISIS data as a reduction of the plasmapause to $L_{\mathrm{P}} < 4$ by the end of day 17.

It is worth noting that our simple procedure identifies the peaks of a flux-versus-L^* profile containing the superposition of outer belt 1 and outer belt 2 populations. One complication of this procedure is that for profiles in which the two populations overlap, there is some inevitable contamination that may lead to errors in the peak and edge locations. Future studies may address this error by modeling the two belts as a superposition of two distinct/separable flux curves.

3. Plasmapause and Outer Belts

In this section we quantify the spatial relationship between the plasmapause and outer belts. We first compare the boundary locations extracted in the previous section, and then compare relativistic electron fluxes to cold plasma density.

3.1. Comparison of Boundary Locations

Figure 5 compares REPT electron peaks (L_{peak}) and edges (L_{edge}) to the EMFISIS-derived plasmapause (L_{P}). Each plot is formatted the same as Figure 4a, with the addition of the plasmapause (thick white line). Five energies are shown.

The energy-dependence of the two outer belts is evident in these plots: the electron population composing outer belt 1 is spectrally much harder than that of belt 2. Belt 1 electrons have significant fluxes in the higher-energy channels, whereas belt 2 is absent above 2.6–3.4 MeV. This energy dependence is discussed further in Section 5.

The spatial relationship between the plasmapause and these two outer belts is also evident. Outer belt 2 is located within one L^* shell of the time-dependent plasmapause. Outer belt 1 is generally deep inside the plasmapause, and its location is uncorrelated with the time-dependent plasmapause. This spatial relationship is further quantified in Figure 6. We follow *O'Brien et al.* [2003] and compare the peak of the outer belt(s) with the plasmapause, though other previous studies have chosen the inner edge of the outer belt for comparison. In Figure 6a through 6e are plotted the difference between the outer belt locations and the plasmapause, $\Delta L^* \equiv L_{\text{peak}} - L_{\text{P}}$, for five energies, and both outer belts. Outer belt 1 is given by the blue curve, and outer belt 2 is red. Where $\Delta L^* < 0$, the outer belt lies within the plasmapause. For each of these curves, the dashed line gives the per-energy mean value ($\langle \Delta L^* \rangle$) during 15–20 January 2013. Figure 6f plots these mean values versus energy.

For this 5-day period, on average, outer belt 1 was well inside the plasmapause; $\langle \Delta L^* \rangle$ exhibits a shallow drop from -1.3 to -1.8 with energy between 1.8 MeV and 7.7 MeV. Thus, the location of the peak flux in belt 1 seems weakly dependent on energy, but independent of the plasmapause location. In contrast, the location of outer belt 2 does appear to be correlated with the plasmapause. At all energies for which there is an outer belt 2, $|\langle \Delta L^* \rangle| \leq 0.5$.

3.2. Comparison of Fluxes and Densities

Figure 7 plots relativistic electron flux (f) versus cold plasma density (n), at four selected energies, and during two selected time intervals (during which L_{peak} and L_{edge} locations were relatively steady). The blue data are for outer belt 1, and the red data are for belt 2. Flux data points are only plotted if their corresponding spin-averaged count rates were above 25 s^{-1}. Flux values were assigned to each belt (1 or 2) if their bin locations fell within the range $L_{\text{edge}} \leq L \leq L_{\text{peak}}$. Thus, these fluxes are from the region earthward of the peak, where $d \log f / dL^* > 0$.

For each energy the thick line gives an empirical linear fit to $\log f$ versus $\log n$, except for the 2.6 and 3.4 MeV plots for outer belt 2 that have too few points. The linear fit is weighted, using measurement errors of $C^{-0.5}$, where C is the count rate for each binned flux. Each plot is annotated (upper left corner) with its fit parameters. All fitted slopes are negative; i.e., electron fluxes earthward of each belt's peak are anti-correlated with cold plasma density.

An inverse relationship might be expected because the plasmasphere hosts a major loss term (hiss), and is generally spatially complementary with a major energization term (chorus). However, the comparison should be performed for a larger dataset to demonstrate statistical significance. Moreover, sampling points earthward of the peak may yield an inverse relationship in part because cold density generally falls with L. To test this factor, we repeated the above analysis for outer belt 1, at 1.8 and 2.1 MeV, for post-disturbance fluxes within the range $L_{\mathrm{peak}} \leq L \leq L_{\mathrm{edge}}$ (i.e., at the outer, negative flux gradient $d \log f / dL^* < 0$). The alternate calculation (not shown), which samples the outer edge of outer belt 1, rather than the inner edge, also exhibits an inverse relationship similar to that shown in Figure 7.

4. Global Context: PTP Model

In this section we use a model to provide global context for the local observations by the Van Allen Probes. The model is a plasmapause test particle (PTP) dynamic simulation that represents the plasmaspheric boundary as an ensemble of $E \times B$-drifting particles, as described in more detail in earlier papers [*Goldstein et al.*, 2005a, 2014a]. The PTP simulation's electric field is driven by the solar wind E-field and Kp. The simulation run for the 15–20 January 2013 event was reported by *Goldstein et al.* [2014b].

Figure 8a plots the locations of Van Allen Probes A plasmapause encounters during 15–20 January. The black line gives the plasmapause locations obtained from the EMFISIS binned densities by the automated algorithm (cf. Section 2.3). The blue line shows plasmapause locations encountered by a virtual satellite flying through the PTP simulation [*Goldstein et al.*, 2014b], also binned to match the time cadence and L^* resolution of the REPT spectrograms. The dashed lines give the averages for the EMFISIS and PTP curves; these mean values agree to within 0.4 R_E, which increases confidence that the global context provided by the simulation may be useful for the observations.

Figure 8b shows the magnetic local time (MLT) extent of the plasmasphere versus time, at $L = 5$, as follows. At each time (horizontal axis), the vertical dimension is colored green to indicate the region inside the plasmapause. For example, snapshots at two selected times are given in Figure 8d. The first snapshot is from 2210 UT on 17 January. At $L = 5$ (dashed blue line), the model plasmasphere region is roughly between noon (1200 MLT) and dusk (1800 MLT). This time (2210 UT, 17 January) is indicated by a black vertical line in Figure 8b. Along this line the green region spans 1200–1800 MLT. The second snapshot (0135 UT, 19 January, cf. Figure 8c) has a more complicated plasmapause shape with a residual wrapped plume [*Goldstein et al.*, 2014b], leading to several regions of green along the corresponding black vertical line in the MLT-versus-time plot.

We now introduce a new plasmaspheric index, the fraction inside the plasmasphere (F_p). The F_p index is simply the fraction of a circular drift orbit that lies within the plasmasphere, which because of the dynamically-changing plasmapause shape, generally depends both on L-value and time. More earthward circles may lie entirely inside the plasmasphere ($F_p = 1$), whereas farther out, circular drift orbits might only cross a plume ($F_p < 1$) or no cold plasma at all ($F_p = 0$). The blue curve of Figure 8b gives the F_p index for $L = 5$, versus time. Again using the example at 2210 UT on 17 January (black vertical line), the cold plasma at $L = 5$ spanned 1200–1800 MLT, i.e., 6 MLT hours, or $F_p = 0.25$.

The model-derived F_p index is intended to provide a metric of the per-L^*, globally-integrated opportunity for losses in the cold plasma. For relativistic electrons with nearly circular drift orbits, the F_p index measures the fraction of their path within the plasmasphere; for constant drift speed this would also be the fraction of their time. Figure 8c plots the F_p index versus L^* and time. Dark green gives $F_p \sim 1$. White regions are where electrons spend approximately half of their orbit inside the plasmasphere. Blue regions show $F_p < 0.4$. The PTP model's virtual-satellite plasmapause (black curve) approximately follows the general shape of the $F_p \geq 0.6$ region. Because F_p is a global index, correspondence with the black curve means that the simulated "local" plasmapause encounters (measured along the virtual-satellite trajectory) are a reasonable proxy for the global plasmasphere. Since the EMFISIS-derived local plasmapause locations agree (within 0.4 R_E) with these simulated local crossings, these observed locations are also (by the transitive relation) good proxies for the global plasmasphere, for this event.

Figure 9 plots relativistic electron fluxes versus the F_p plasmaspheric index, at two selected energies, and during two selected time intervals. As for Figure 7, flux values were assigned to belt 1 or 2 from the region earthward of the peak ($d\log f/dL^* > 0$). For outer belt 1 (blue data), the locations earthward of the peak are almost entirely within the plasmasphere, i.e., $F_p = 1$; thus, the electron fluxes are uncorrelated with F_p. In contrast, in outer belt 2 flux drops with increasing F_p. Note that because data fall into two distinct groups above and below the value $F_p \sim 0.4$, two slightly different linear fits are shown for belt 2. The solid lines are the fits for the range $F_p = [0.4, 0.99]$; these fit parameters annotate the upper left corner. The dashed lines give fits for a wider range $F_p = [0.15, 0.99]$, which yield slopes of -0.4 and -0.5 respectively for 1.8 and 2.1 MeV.

Both these ranges yield negative slopes, implying that electrons on orbits with greater plasmaspheric overlap experience greater cumulative scattering losses.

The F_p index thus has two possible uses. First, it provides a way to determine if in situ measurements may be used as a proxy for the global region of cold plasma encountered by relativistic electrons. Second, if boundary locations are available but densities are not, F_p may help measure (e.g., as a negative slope in Figure 9) the net, time-integrated effect of losses inside the plasmasphere.

5. Interpretation

Our analysis of the 15–20 January 2013 time interval confirms the preliminary conclusion [*Baker et al.*, 2013; *Hudson et al.*, 2014; *Baker et al.*, 2014] that the spatial relationship between the plasmapause and outer belt region may be more complicated than the simple picture in which the outer belt peak lines up with the plasmapause [*O'Brien et al.*, 2003; *Goldstein et al.*, 2005c; *Li et al.*, 2006]. We found a strongly location- and energy-dependent response. Prior to the 17 January disturbance, there were two outer zones of relativistic electrons, which we labeled belt 1 and belt 2. Belt 1 consisted of higher-energy ($>$ 3 MeV) electrons deep inside the plasmasphere. Belt 2 was lower-energy ($<$ 3 MeV) electrons whose peak location roughly (within 0.5 R_E) followed the plasmapause. After the disturbance the partially-depleted belt 1 flux decayed, whereas belt 2 flux recovered after the factor-of-100 disturbance-time dropout. As discussed in the following sections, outer belt 2 bears the typical relationship to the plasmapause in which the electron peak is correlated with the plasmapause, whereas the dynamics of outer belt 1 is indicative of the more atypical storage-ring configuration.

5.1. Outer Belt 1 (Storage Ring)

The presence of belt 1 deep within the plasmasphere represents the more atypical storage-ring configuration, i.e., an energetic outer belt with significant plasmaspheric overlap on long time scales. How do we explain the belt 1 observations? Our interpretation is that the dynamics of outer belt 1 during 15–20 January resulted from the combined influence of at least two phenomena: plasmaspheric hiss before and after the disturbance, and modest (though rapid) losses during the disturbance.

In the pre-disturbance outer belt 1, the electron loss timescales are consistent with those of plasmaspheric hiss. Figure 10a depicts the time development of electron flux for selected energies spanning 1.8–6.3 MeV, at $L^* = 3.5$; i.e., at an L^* value representative of outer belt 1 before the disturbance. At each energy the log flux before day 17 is fitted to an $\exp(-t/\tau)$ dependence; this fit is given in the log-scaled plot by the thick straight line. The fitted values of the loss timescale τ (cf. annotation to the left of each flux curve) increase with energy, from 10 d at 1.8 MeV to 129 d at 6.3 MeV. Thus, the decay before the disturbance was stronger at lower energies, at $L^* = 3.5$. Figure 10b repeats this loss timescale calculation at binned L^* values between 3 and 5. Negative τ values found outside of $L^* \sim 4.2$ or so (i.e., in outer belt 2) are not plotted. At each energy the electron lifetimes vary by a factor of ∼4. Nonetheless, the lifetime curves for each L^* value rises steeply with energy, from 8–33 d at 1.8 MeV to 45–130 d at 6.3 MeV. These electron lifetimes (including their energy dependence) are very consistent with theoretical predictions of hiss loss timescales at $L = 3.2$ by *Ni et al.* [2013]. *Meredith et al.* [2007] also predicted hiss lifetimes (at $L = 3.5$ and for AE<100 nT) similar to our measured lifetimes: 20 d (> 100 d) for 2 MeV (5 MeV).

Electron loss timescales in the post-disturbance outer belt 1 are also consistent with those of plasmaspheric hiss. As was done for the pre-disturbance data, in Figure 10c at each energy the log flux (after day 18) is fitted to an $\exp(-t/\tau)$ dependence. The resultant electron lifetimes increase with energy, from 10 d at 1.8 MeV to 73 d at 6.3 MeV. Figure 10d plots the electron lifetimes versus energy and L^*, and as with the pre-disturbance data these lifetimes are very consistent with those for plasmaspheric hiss.

EMFISIS observations of plasmaspheric hiss throughout the 5-day interval support this interpretation. Figure 11 plots an order-of-magnitude estimate of hiss wave power (cf. Appendix A2) versus time for 15–20 January. The thick gray line plots the peak value per 9-h interval; purple number labels indicate power levels (in $\mathrm{nT}^2 \times 10^4$), rounded to one significant digit. Significant hiss wave power was observed both before and after the 17 January disturbance, though the peak wave power was generally higher afterward; the per-day maximum on day 17 was a factor of $\sim$5 higher than the previous day. The red numbers at the top of the plot indicate the corresponding hiss amplitudes (in pT), which are in the correct range to be responsible for the observed electron loss timescales of both Figure 10b (before the disturbance) and Figure 10d (after).

As shown in Figure 12, belt 1 exhibited only a modest flux dropout during the disturbance, strongest in the $\sim$3–5 MeV energy range. This dropout is discussed in Section 5.2.

Outer belt 1 observations are thus consistent with the behavior and properties of a storage ring [*Baker et al.*, 2013]: a long-lived, energetic belt deep inside the plasmasphere. Prior to the disturbance it was already slowly decaying at an energy-dependent rate consistent with scattering by hiss; after the disturbance-time depletion it continued to decay at a nearly identical rate. The peak electron fluxes, at several MeV, have lifetimes of weeks (or even months). Left undisturbed, as for example during prolonged intervals of relatively quiet conditions with no significant plasmapheric erosion, these storage rings can persist for a long time, as previously noted by *Baker et al.* [2014]. Indeed in the 1.5 months preceding our case study (i.e., between 1 December 2012 and 16 January 2013), very quiet conditions prevailed with Dst> -30 nT. Extra shielding may be provided by the plasmasphere [*Turner et al.*, 2014a] during isolated solar wind pressure increases.

5.2. Disturbance-Time Losses

The flux dropouts recorded after the 17 January disturbance are consistent with an outer magnetospheric loss process. Disturbance-related dropouts were large outside the plasmapause, and small inside.

Figure 12b shows flux versus time at selected energies, at $L^* = 4.7$, i.e., in outer belt 2, and outside the plasmapause ($L_{\mathrm{P}} \approx 4.4$ at the time of the belt 2 dropout). After the disturbance, fluxes at $L^* = 4.7$ dropped by as much as two orders of magnitude. Figure 12a shows flux at $L^* = 3.5$, i.e., in outer belt 1, and inside the plasmapause ($L_{\mathrm{P}} \approx 3.8$ at the time of the belt 1 dropout). At this lower L^* value the fluxes dropped by a more modest factor of $<$ 2–4 at all energies, and the dropouts happened later than at higher L^*. To quantify the magnitude of the dropouts more systematically, Figures 12c and 12d plot the dropout flux ratio R_D for outer belts 1 and 2 respectively, versus energy and L^* (the latter being color-coded). Here R_D is defined as the ratio of pre-disturbance to post-disturbance flux. There is a clear progression from larger dropouts at higher L^* to smaller dropouts at more earthward locations. There is also a clear energy dependence. For outer belt 1 at $L^* < 4.2$, the magnitude of the dropout was generally largest in the range ∼3–5 MeV. For outer belt 2 at $L^* \geq 4.2$, the magnitude of the dropout decreased with energy. As discussed below (cf. Section 5.4), in the REPT energy range outer belts 1 and 2 peaked at approximately 3–5 MeV and 1.8 MeV respectively. Thus, for each belt the dropout was largest for energies in the vicinity of the flux-versus-energy peak.

What loss process(es) might yield these spatial and energy dependences? One candidate is magnetopause shadowing. Strong losses in the outer magnetosphere are consistent with outward radial diffusion driven by magnetopause shadowing losses that create a steep gradient in phase space density [*Shprits et al.*, 2006]. Partial shielding by the plasmasphere is also consistent with this mechanism [*Turner et al.*, 2014a]. Next we consider the adiabatic (Dst) response. We do not herein convert flux to phase space density in terms of the adiabatic invariants, as is necessary to quantify the contribution of the adiabatic effect. However, it is possible that some of the outer belt 2 dropout was caused by the adiabatic effect, based on the fact that outer belt 2 recovered to nearly the pre-disturbance flux level within one day (2.5 orbits), which is the same time frame as the recovery to pre-disturbance Dst levels from the moderate minimum of ~ -50 nT. On the other hand, outer belt 1 did not recover at all; after the disturbance, belt 1 decayed from its post-dropout level (as described above). Moreover, BARREL balloon observations indicate electron precipitation (i.e., actual losses, as opposed to adiabatic variation) occurred during 17–19 January 2013 [*Li et al.*, 2014b; *Woodger et al.*, 2015; *Blum et al.*, 2015]. Wave observations during the disturbance suggest EMIC waves may have been responsible for at least some of these losses [*Li et al.*, 2014b; *Blum et al.*, 2015]. Lastly, we consider chorus waves. Figure 13 plots an order-of-magnitude estimate of chorus wave power versus time for 15–20 January, derived from EMFISIS wave observations (cf. Appendix A3). Chorus wavese were observed along the Van Allen Probes A orbit beginning at about 1800 UT on 17 January, i.e., 4.5 hours after the 1330 UT disturbance onset (solid black vertical line). After 1800 UT, wave power peaked at 10^{-3}–10^{-1} nT^2 (i.e., 10^3–10^5 pT^2). *Shprits et al.* [2007] estimated that for chorus of this intensity, >1 MeV electrons have loss timescales of >1 day. Though there may very well have been chorus wave power at other locations (i.e., not along the satellite orbit), the few-hour timescale for the flux dropout of outer belt 2 (Figure 12b) suggests chorus is not the main loss mechanism at work.

5.3. Outer Belt 2 Dynamics

The correlation between the peak of outer belt 2 and the plasmapause follows the typical relationship found in pre-Van-Allen-Probes studies (discussed earlier). This plasmapause-outer belt correspondence is usually attributed to the interplay of both acceleration and loss processes. As the plasmasphere is eroded, the region where loss mechanisms (hiss, EMIC) are effective may likewise shrink. At the same time, acceleration mechanisms outside the plasmapause (chorus waves, Pc5 ULF waves) may also migrate earthward during erosion events. For example, following the disturbance-time dropout of outer belt 2 (Section 5.2), outer belt 2 recovered, essentially regaining its pre-disturbance flux levels within ∼24 hours (cf. Figure 12b). The recovered belt 2 peak was within 0.5 R_E of the plasmapause. One likely mechanism for this recovery is local acceleration by chorus waves just outside the plasmapause. As noted above, moderate-to-strong (10^{-3}–10^{-1} nT^2) chorus wave power was observed by Van Allen Probes A after ∼1800 UT on 17 January (cf. Figure 13). From theoretical calculations by *Summers et al.* [2007], at $L^* = 4.5$ and for wave power of 0.01 nT^2 (in the middle of the range of chorus power observed for our event by Van Allen Probes), the minimum acceleration timescale for $>$ 1 MeV particles is indeed on the order of a day. However, such a short (∼24-hour) recovery time as was observed after the 17 January disturbance is theoretically predicted to result from strong chorus wave activity. Given that the average chorus wave power during the 17–18 January recovery was only moderate (although there were intervals of intense chorus; cf. Figure 13), there was probably at least a partial contribution from the adiabatic effect and/or energization by ultra-low-frequency (ULF) waves [*Hudson et al.*, 1995; *Li et al.*, 1998; *Elkington et al.*, 2003; *Horne et al.*, 2007]. Both chorus and ULF waves are believed to be strongly affected (in terms of wave intensity and propagation) by the evolving cold plasma.

Just before the disturbance, outer belt 2 dynamics was not strongly coupled to that of the plasmasphere. In the ∼12 hours preceding the convection increase of 1330 UT on 17 January, the 1.8–2.1-MeV electrons in outer belt 2 migrated inward (and increased in flux), from $L^* \approx 5.5$ to $L^* \approx 4.7$ (cf. Figure 5a and Figure 5b). This inward migration was probably caused by the elevated solar wind pressure that began early on 17 January (cf. Figure 1). Some energization occurred as well; the pressure enhancement was accompanied by a sharp increase in fluxes of 2.6–3.4 MeV electrons at $L^* \approx 4.7$, whereas prior to the pressure increase belt 2 fluxes were not significant at these energies (cf. Figure 5c and Figure 5d). During this belt 2 inward migration, the plasmapause instead moved outward (cf. Figure 5a).

5.4. Energetics of Outer Belts 1 and 2

Figure 14 plots electron flux versus energy and L^* at two selected times before and after the disturbance. With a local flux maximum at ∼3–5 MeV, belt 1 was more energetic than belt 2, whose flux (in the REPT energy range) decreased steeply with energy above

1.8 MeV. Figure 14 shows that the net effect of the day 17 disturbance was to reduce the flux of < 4 MeV electrons in outer belt 1, and move both belts inward, as follows. After day 18, outer belt 1 (partially depleted at all energies) decayed at rates favoring higher losses at lower energies. Belt 1 experienced a net migration from an energy-averaged location of $L^* = 3.4$ to $L^* = 3.2$ ($\Delta L^* = -0.2$). Belt 2 also moved inward, from $L^* = 5.1$ to $L^* = 4.6$ ($\Delta L^* = -0.5$), but recovered its pre-event flux and flux-versus-energy distribution.

6. Summary

In this paper we have studied an atypical outer belt morphology during a five-day period, 15–20 January 2013, by comparing the locations of relativistic electron peaks to the plasmapause. At the start of the interval there were two pre-existing outer belts, a stable zone deep within the plasmasphere (belt 1) and a more dynamic zone near the plasmapause (belt 2). Belt 2 was emptied out during the disturbance, possibly by magnetopause shadowing with some contribution from the adiabatic effect, but was restored within 24 hours. Belt 1 was slowly decaying on hiss timescales before the disturbance, and suffered only a modest dropout, perhaps owing to shielding from radial diffusion by the plasmasphere. After the disturbance, the partially-depleted belt 1 continued to decay at the same rate as before.

We quantified the spatial relationship between the plasmapause and outer belt electrons for the 15–20 January interval, by comparing the locations of relativistic electron peaks in both belts to the plasmapause. We found that the stable, more energetic outer belt 1 was (on average) between 1 and 2 R_E inside the plasmapause, with deeper penetration into cold plasma for higher energies. The dynamic outer belt was (on average) within 0.5 R_E of the moving plasmapause. Relativistic electron fluxes earthward of each belt's peak were found to be anti-correlated with cold plasma density, implying that electrons immersed in denser plasma experience greater cumulative scattering losses (or lesser cumulative acceleration).

To provide global context for our data analysis, we used a plasmapause test particle (PTP) simulation. Virtual satellite crossings of the simulated plasmapause agree (on average) with actual crossings to within 0.4 R_E. We introduced a new plasmaspheric index F_p, the fraction of a circular drift orbit inside the plasmapause. Based on agreement between regions of high F_p and the virtual satellite crossings we concluded that the locally-measured plasmapause is (for this event) a good proxy for the per-L^*, globally-integrated opportunity for losses in the cold plasma.

Our analysis of the 15–20 January 2013 time interval confirms that the spatial relationship between the plasmapause and outer belt region may be more complicated than was generally believed before the Van Allen Probes mission. This single case study is the first step in determining and understanding that complexity. The next step will require a systematic study such as that of *Li et al.* [2006], but using Van Allen Probes data. The automated techniques used herein (to obtain electron peaks and edges, and plasmapause locations) lend themselves to a more systematic, statistical study using a larger dataset. Extending the energy range to lower energies is also necessary to understand more fully the role of hiss.

Appendix A: EMFISIS Wave Data Analysis

In this appendix we describe how Van Allen Probes EMFISIS wave data are analyzed to obtain electron number density, and identify plasmaspheric hiss. The former is obtained from the High Frequency Receiver (HFR), and the latter from the Waveform Receiver (WFR) [*Kletzing et al.*, 2013].

A1. Electron Number Density

This subsection is a brief description of how EMFISIS plasma wave data are analyzed to obtain electron number density. A more complete description is contained in *Goldstein et al.* [2014b].

Electron number density is obtained from EMFISIS HFR data as shown in Figure A.1a. For each HFR spectrogram, the upper hybrid resonance (UHR) line [*Mosier et al.*, 1973] is manually identified, and the electron plasma frequency ($f_{\rm pe}$) is assumed to lie at the UHR lower edge. Values of $f_{\rm pe}$ are extracted manually, using the CURSOR routine of the Interactive Data Language (IDL). Each manually-clicked point is reassigned to the center of the nearest pixel, yielding an extraction binned to the UT cadence and frequency resolution of the HFR. These plasma frequencies are converted to number density using the standard formula $n_e(\,{\rm cm}^{-3}) = (f_{\rm pe}/8979.49{\rm Hz})^2$, as shown in Figure A.1b. *Goldstein et al.* [2014b] showed that these manually-extracted n_e values agreed with those obtained using a semi-automated algorithm, to within 9% on average, i.e., to within < 1 HFR frequency bin.

A2. Plasmaspheric Hiss

This subsection describes how plasmaspheric hiss signals are herein identified from EMFISIS WFR data from 15–20 January 2013. Hiss is a broad-band electromagnetic wave observed in plasmaspheric plasma, in the ∼100 Hz to ∼1 kHz range and having peak amplitudes in the ∼100 pT range [*Thorne et al.*, 1973; *Meredith et al.*, 2004; *Bortnik et al.*, 2008]. Proper extraction from wave data requires wave polarization analysis to distinguish plasmaspheric hiss from other wave modes such as magnetosonic waves [*Li et al.*, 2015a]. In this appendix we present a fast, crude identification algorithm based solely on the known average spectral properties (frequency range) and occurrence location (inside the plasmasphere). The purpose of this hiss extraction is solely to obtain an order-of-magnitude estimate of the hiss wave power for our case study of the 15–20 January 2013 event.

For illustrative purposes, an example spectrogram of WFR data ($B_u B_u$ component) spanning 16–18 January is shown in Figure A.2b. For this study, the WFR data are filtered using a semi-automated algorithm, as follows. High-density regions are first determined using extracted electron number densities (Figure A.2a). To filter out non-plasmaspheric intervals, an ad-hoc upper frequency cutoff is assumed to follow $10 n_e \times \text{cm}^3\text{Hz}$ (Figure A.2b). The lower frequency threshold is set to a nominal/conservative value of 100 Hz. After this automatic filtering, a manual filter is applied to remove 21 specific UT intervals: Day 15: 0000–0036, 0106–0200, 0254–0318, 0500–0818, 1030–1100, 1930–2000, 2200–0000; Day 16: 0000–0242, 0448–0500, 0612–1000, 1800–0000; Day 17: 0400–0718, 1630–0000; Day 18: 0130–1030, 1912–0000; Day 19: 0000–0248, 0430–0500, 0606–1130, 1312–1342, 1718–2000, 2242–0000. The resulting filtered WFR spectrogram is shown in Figure A.2b. The frequency-integrated wave power (Figure A.2c) is then calculated using the INT_TABULATED routine in IDL. To check the extraction, our filtered spectrogram of 16 January was compared to that obtained for the same day by *Li et al.* [2015a] using a more rigorous wave polarization analysis. For 16 January our method agreed qualitatively with the wave-polarization method, well enough to provide an order-of-magnitude estimate for hiss wave power.

The wave power curve (Figure A.2c) is in the range expected for hiss (peak power ~ 0.01 nT^2), although there may be a finite contribution from magnetosonic waves. The analysis demonstrates that plasmaspheric hiss was present in the plasmasphere both before and after the disturbance (1330 UT on 17 January; cf. Section 2.1). The peak per-day hiss wave power increased from 4×10^{-3} nT^2 on day 16, to 2×10^{-2} nT^2; i.e., by a factor of 5.

A3. Chorus

This subsection describes how chorus wave signals are analyzed from EMFISIS WFR data from 15–20 January 2013. Chorus is an intense, whistler-mode wave usually observed outside the plasmapause, in the ∼0.1–0.8 f_{ce} range (where f_{ce} is the electron cyclotron frequency), whose wave power depends on the geomagnetic disturbance level [*Burtis and Helliwell*, 1969; *Meredith et al.*, 2001; *Li et al.*, 2013]. In this appendix we present our technique for identifying and estimating chorus wave power for our case study of the 15–20 January 2013 event.

Figure A.3a shows an example EMFISIS WFR spectrogram ($B_u B_u$ component) spanning 16–18 January, manually filtered to remove all but intervals containing significant chorus wave power. From this spectrogram, chorus magnetic wave power is calculated by numerically integrating the spectral density from the lower hybrid frequency to 0.8 f_{ce}. The resultant wave power is shown in Figure A.3b. These local measurements (taken along the Van Allen Probes A orbital trajectory) indicate that moderate to strong chorus wave power was observed late in the day (after about 1800 UT) on 17 January 2013. *Li* *et al.* [2013] demonstrated how electron data from low-altitude satellites can be analyzed to infer global chorus wave amplitudes. We applied this technique (results not included here) to find at least moderate chorus wave power, outside the Van Allen Probes observed plasmapause at a range of MLT values spanning the postmidnight to prenoon sectors.

Acknowledgments.

Van Allen Probes data (and plasmapause test particle simulations) are publicly accessible via the ECT and EMFISIS links at http://rbspgway.jhuapl.edu/. OMNI solar wind data are accessible via http://cdaweb.gsfc.nasa.gov/. This work was supported primarily by RBSP-ECT funding provided by JHU/APL contract 967399 under NASA's prime contract NAS5-01072. Development of the FIDO index was supported by the NASA Heliophysics Guest Investigator pro- gram under NNX07AG48G. The research at University of Iowa was supported by JHU/APL contract 921647 under NASA prime contract NAS5-01072. The analysis at UCLA was supported by NASA grant NNX15AF61G and AFOSR award FA9550-15-1-0158. OMNI 5-min data, provided by J. H. King, N. Patatashvilli at AdnetSystems, NASA GSFC and CDAWeb, were derived from datasets produced by the Wind and ACE missions.

References

Baker, D. N., J. B. Blake, L. B. Callis, J. R. Cummings, D. Hovestadt, S. Kanekal, B. Klecker, R. A. Mewaldt, and R. D. Zwicki (1994), Relativistic electron acceleration and decay time scales in the inner and outer radiation belts: SAMPEX, *Geophys. Res. Lett.*, *21*, 409.

Baker, D. N., S. G. Kanekal, X. Li, S. P. Monk, J. Goldstein, and J. L. Burch (2004), An extreme distortion of the Van Allen belt arising from the 'Halloween' solar storm in 2003, *Nature*, *432*, 878, doi:10.1038/nature03116.

Baker, D. N., et al. (2013), A long-lived relativistic electron storage ring embedded in Earth's outer Van Allen Belt, *Science*, *340*, 186, doi:10.1126/science.1233518.

Baker, D. N., et al. (2013), The Relativistic Electron-Proton Telescope (REPT) Instrument on Board the Radiation Belt Storm Probes (RBSP) Spacecraft: Characterization of Earth's Radiation Belt High-Energy Particle Populations, *Space Sci. Rev.*, *179*, 337–381, doi:10.1007/s11214-012-9950-9.

Baker, D. N., et al. (2014), An impenetrable barrier to ultrarelativistic electrons in the Van Allen radiation belts, *Nature*, *515*, 531, doi:10.1038/nature13956.

Blum, L. W., et al. (2015), Observations of coincident EMIC wave activity and duskside energetic electron precipitation on 18-19 January 2013, *Geophys. Res. Lett.*, *42*, 5727, doi:10.1002/2015GL065245.

Borovsky, J. E., R. H. W. Friedel, and M. H. Denton (2014), Statistically measuring the amount of pitch angle scattering that energetic electrons undergo as they drift across the plasmaspheric drainage plume at geosynchronous orbit, *J. Geophys. Res.*, *119*, 1814, doi:10.1002/2013JA019310.

Bortnik, J., R. M. Thorne, and N. P. Meredith (2008), The unexpected origin of plasmaspheric hiss from discrete chorus emissions, *Nature*, *452*, 62, doi:10.1038/nature06741.

Breneman, A. W., et al. (2015), Global-scale coherence modulation of radiation-belt electron loss from plasmaspheric hiss, *Nature*, *523*, 193, doi:10.1038/nature14515.

Burtis, W. J., and R. A. Helliwell (1969), Banded chorus: A new type of VLF radiation observed in the magnetosphere by OGO 1 and OGO 3, *J. Geophys. Res.*, *74*, 3002, doi:10.1029/JA074i011p03002.

Chappell, C. R. (1974), Detached plasma regions in the magnetosphere, *J. Geophys. Res.*, *79*, 1861, doi:10.1029/JA079i013p01861.

Chappell, C. R., K. K. Harris, and G. W. Sharp (1970), The morphology of the bulge region of the plasmasphere, *J. Geophys. Res.*, *75*, 3848, doi:10.1029/JA075i019p03848.

Clilverd, M. A., et al. (2015), Electron precipitation from EMIC waves: A case study from 31 May 2013, *J. Geophys. Res.*, *120*, 3618, doi:10.1002/2015JA021090.

Craven, P. D., D. L. Gallagher, and R. H. Comfort (1997), Relative concentration of He^+ in the inner magnetosphere as observed by the DE 1 retarding ion mass spectrometer, *J. Geophys. Res.*, *102*, 2279, doi:10.1029/96JA02176.

Denton, R. E., V. K. Jordanova, and B. J. Fraser (2014), Effect of spatial density variation and O+ concentration on the growth and evolution of electromagnetic ion cyclotron waves, *J. Geophys. Res.*, *119*, 8372, doi:10.1002/2014JA020384.

Drozdov, A. Y., Y. Y. Shprits, K. G. Orlova, A. C. Kellerman, D. A. Subbotin, D. N. Baker, H. E. Spence, and G. D. Reeves (2015), Energetic, relativistic, and ultrarelativistic electrons: Comparison of long-term VERB code simulations with Van Allen Probes measurements, *J. Geophys. Res.*, *120*, 3574, doi:10.1002/2014JA020637.

Elkington, S. R., M. K. Hudson, and A. A. Chan (2003), Resonant acceleration and diffusion of outer zone electrons in an asymmetric geomagnetic field, *J. Geophys. Res.*, *108*, 1116.

Engebretson, M. J., et al. (2015), Van Allen probes, NOAA, GOES, and ground observations of an intense EMIC wave event extending over 12 h in magnetic local time, *J. Geophys. Res.*, *120*, 5465, doi:10.1002/2015JA021227.

Fennell, J. F., S. G. Claudepierre, J. B. Blake, T. P. O'Brien, J. H. Clemmons, D. N. Baker, H. E. Spence, and G. D. Reeves (2015), Van Allen Probes show that the inner radiation zone contains no MeV electrons: ECT/MagEIS data, *Geophys. Res. Lett.*, *42*, 1283, doi:10.1002/2014GL062874.

Fraser, B. J., and T. S. Nguyen (2001), Is the plasmapause a preferred source region of electromagnetic ion cyclotron waves in the magnetosphere?, *J. Atmos. Solar-Terr. Phys.*, *63*, 1225.

Fraser, B. J., H. J. Singer, M. L. Adrian, D. L. Gallagher, and M. F. Thomsen (2005), The Relationship Between Plasma Density Structure and EMIC Waves at Geosynchronous Orbit, in *Inner Magnetosphere Interactions: New Perspectives from Imaging*, edited by J. L. Burch, M. Schulz, and H. Spence, p. 55, American Geophysical Union, Washington, D. C.

Fraser, B. J., R. S. Grew, S. K. Morley, J. C. Green, H. J. Singer, T. M. Loto'aniu, and M. F. Thomsen (2010), Storm time observations of electromagnetic ion cyclotron waves at geosynchronous orbit: GOES results, *J. Geophys. Res.*, *115*, A05208, doi:10.1029/2009JA014516.

Goldstein, J., and B. R. Sandel (2005), The global pattern of evolution of plasmaspheric drainage plumes, in *Inner Magnetosphere Interactions: New Perspectives from Imaging*, edited by J. L. Burch, M. Schulz, and H. Spence, p. 1, American Geophysical Union, Washington, D. C., doi:10.1029/159GM01.

Goldstein, J., J. L. Burch, and B. R. Sandel (2005a), Magnetospheric model of subauroral polarization stream, *J. Geophys. Res.*, *110*, A09222, doi:10.1029/2005JA011135.

Goldstein, J., J. L. Burch, B. R. Sandel, S. B. Mende, P. C:son Brandt, and M. R. Hairston (2005b), Coupled response of the inner magnetosphere and ionosphere on 17 April 2002, *J. Geophys. Res.*, *110*, A03205, doi:10.1029/2004JA010712.

Goldstein, J., S. G. Kanekal, D. N. Baker, and B. R. Sandel (2005c), Dynamic relationship between the outer radiation belt and the plasmapause during March–May 2001, *Geophys. Res. Lett.*, *32*, L15104, doi:10.1029/2005GL023431.

Goldstein, J., M. F. Thomsen, and A. DeJong (2014a), In situ signatures of residual plasmaspheric plumes, *J. Geophys. Res.*, *119*, 4706, doi:10.1002/2014JA019953.

Goldstein, J., et al. (2014b), Simulation of Van Allen Probes plasmapause encounters, *J. Geophys. Res.*, *119*, 7464, doi:10.1002/2014JA020252.

Halford, A. J., B. J. Fraser, and S. K. Morley (2010), EMIC wave activity during geomagnetic storm and nonstorm periods: CRRES results, *J. Geophys. Res.*, *115*, A12248, doi:10.1029/2010JA015716.

Halford, A. J., B. J. Fraser, and S. K. Morley (2015), EMIC waves and plasmaspheric and plume density: CRRES results, *J. Geophys. Res.*, *120*, 1974, doi:10.1002/2014JA020338.

Hardman, R., M. A. Clilverd, C. J. Rodger, J. B. Brundell, R. Duthie, R. H. Holzworth, I. R. Mann, D. K. Milling, and E. Macusova (2015), A case study of electron precipitation fluxes due to plasmaspheric hiss, *J. Geophys. Res.*, *120*, 6736, doi: 10.1002/2015JA021429.

Horne, R. B., R. M. Thorne, S. A. Glauert, J. M. Albert, N. P. Meredith, and R. R. Anderson (2005), Timescale for radiation belt electron acceleration by whistler-model chorus waves, *J. Geophys. Res.*, *110*, doi:10/1029/2004JA010811.

Horne, R. B., R. M. Thorne, S. A. Glauert, N. P. Meredith, D. Pokhotelov, and O. Santolík (2007), Electron acceleration in the Van Allen radiation belts by fast magnetosonic waves, *Geophys. Res. Lett.*, *34*, L17107, doi:10.1029/2007GL030267.

Horwitz, J. L., R. H. Comfort, P. G. Richards, C. M. O., C. R. Chappell, P. Anderson, W. B. Hanson, and L. H. Brace (1990), Plasmasphere-ionosphere coupling 2. Ion composition measurements at plasmaspheric and ionospheric altitudes and comparison with modeling results, *J. Geophys. Res.*, *95*, 7949.

Hudson, M. K., A. D. Kotelnikov, X. Li, I. Roth, M. Temerin, J. Wygant, J. B. Blake, and M. S. Gussenhoven (1995), Simulation of proton radiation belt formation during the March 24, 1991 SSC, *Geophys. Res. Lett.*, *22*, 291.

Hudson, M. K., S. R. Elkington, J. G. Lyon, V. A. Marchenko, I. Roth, M. Temerin, J. B. Blake, M. S. Gussenhoven, and J. R. Wygant (1997), Simulation of radiation belt formation during storm sudden commencements, *J. Geophys. Res.*, *102*, 14087.

Hudson, M. K., D. N. Baker, J. Goldstein, B. T. Kress, J. Paral, F. R. Toffoletto, and M. Wiltberger (2014), Simulated magnetopause losses and Van Allen Probe flux dropouts, *Geophys. Res. Lett.*, *41*, 1113, doi:10.1002/2014GL059222.

Jaynes, A. N., et al. (2014), Evolution of relativistic outer belt electrons during an extended quiescent period, *J. Geophys. Res.*, *119*, 9558, doi:10.1002/2014JA020125.

Johnston, W. R., and P. C. Anderson (2010), Storm time occurrence of relativistic electron microbursts in relation to the plasmapause, *J. Geophys. Res.*, *115*, A02205, doi:10.1029/2009JA014328.

Kersten, T., R. B. Horne, S. A. Glauert, N. P. Meredith, B. J. Fraser, and R. S. Grew (2014), Electron losses from the radiation belts caused by EMIC waves, *J. Geophys. Res.*, *119*, 8820, doi:10.1002/2014JA020366.

Kim, K.-C., D.-Y. Lee, and Y. Shprits (2015), Dependence of plasmaspheric hiss on solar wind parameters and geomagnetic activity and modeling of its global distribution, *J. Geophys. Res.*, *120*, 1153, doi:10.1002/2014JA020687.

Kletzing, C. A., et al. (2013), The Electric and Magnetic Field Instrument Suite and Integrated Science (EMFISIS) on RBSP, *Space Sci. Rev.*, *179*, 127–181, doi:10.1007/s11214-013-9993-6.

Lemaire, J. F., and K. I. Gringauz (1998), *The Earth's Plasmasphere*, Cambridge University Press, Cambridge.

Lepping, R. P., et al. (1995), The WIND Magnetic Field Investigation, *Space Sci. Rev.*, *71*, 207.

Li, W., B. Ni, R. M. Thorne, J. Bortnik, J. C. Green, C. A. Kletzing, W. S. Kurth, and G. B. Hospodarsky (2013), Constructing the global distribution of chorus wave intensity using measurements of electrons by the POES satellites and waves by the Van Allen Probes, *Geophys. Res. Lett.*, *40*, 4526, doi:10.1002/grl.50920.

Li, W., Q. Ma, R. M. Thorne, J. Bortnik, C. A. Kletzing, W. S. Kurth, G. B. Hospodarsky, and Y. Nishimura (2015a), Statistical properties of plasmaspheric hiss derived from Van Allen Probes data and their effects on radiation belt electron dynamics, *J. Geophys. Res.*, *120*, 3393, doi:10.1002/2015JA021048.

Li, W., et al. (2014a), Quantifying hiss-driven energetic electron precipitation: A detailed conjunction event analysis, *Geophys. Res. Lett.*, *41*, 1085, doi:10.1002/2013GL059132.

Li, X., D. Baker, M. Temerin, G. D. Reeves, and R. D. Belian (1998), Simulation of dispersionless injections and drift echoes of energetic electrons associated with substorms, *Geophys. Res. Lett.*, *25*, 3763.

Li, X., D. N. Baker, T. P. O'Brien, L. Xie, and Q. G. Zong (2006), Correlation between the inner edge of outer radiation belt electrons and the innermost plasmapause location, *Geophys. Res. Lett.*, *33*, L14107, doi:10.1029/2006GL026294.

Li, X., R. S. Selesnick, D. N. Baker, A. N. Jaynes, S. G. Kanekal, Q. Schiller, L. Blum, J. Fennell, and J. B. Blake (2015b), Upper limit on the inner radiation belt MeV electron intensity, *J. Geophys. Res.*, *120*, 1215, doi:10.1002/2014JA020777.

Li, Z., et al. (2014b), Investigation of EMIC wave scattering as the cause for the BARREL 17 January 2013 relativistic electron precipitation event: A quantitative comparison of simulation with observations, *Geophys. Res. Lett.*, *41*, 8722, doi:10.1002/2014GL062273.

Lorentzen, K. R., M. P. McCarthy, G. K. Parks, J. E. Foat, R. M. Millan, D. M. Smith, R. P. Lin, and J. P. Treilhou (2000), Precipitation of relativistic electrons by interaction with electromagnetic ion cyclotron waves, *J. Geophys. Res.*, *105*(A3), 5381, doi: 10.1029/1999JA000283.

Loto'aniu, T. M., B. J. Fraser, and C. L. Walters (2005), Propagation of electromagnetic ion cyclotron wave energy in the magnetosphere, *J. Geophys. Res.*, *110*, A07214, doi: 10.1029/2004JA010816.

Loto'aniu, T. M., R. M. Thorne, B. J. Fraser, and D. Summers (2006), Estimating relativistic electron pitch angle scattering rates using properties of the electromagnetic ion cyclotron wave spectrum, *J. Geophys. Res.*, *111*, A04220.

Lyons, L. R., and R. M. Thorne (1973), Equilibrium structure of radiation belt electrons, *J. Geophys. Res.*, *78*, 2142.

Lyons, L. R., R. M. Thorne, and C. F. Kennel (1972), Pitch-angle diffusion of radiation belt electrons within the plasmasphere, *J. Geophys. Res.*, *77*, 3455.

Ma, Q., et al. (2015), Modeling inward diffusion and slow decay of energetic electrons in the Earth's outer radiation belt, *Geophys. Res. Lett.*, *42*, 987, doi:10.1002/2014GL062977.

Mauk, B. H., N. J. Fox, S. G. Kanekal, R. L. Kessel, D. G. Sibeck, and A. Ukhorskiy (2013), Science Objectives and Rationale for the Radiation Belt Storm Probes Mission, *Space Sci. Rev.*, *179*, 3–27, doi:10.1007/s11214-012-9908-y.

Meredith, N. P., R. B. Horne, and R. R. Anderson (2001), Substorm dependence of chorus amplitudes: Implications for the acceleration of electrons to relativistic energies, *J. Geophys. Res.*, *106*, 13165–13178.

Meredith, N. P., R. M. Thorne, R. B. Horne, D. Summers, B. J. Fraser, and R. R. Anderson (2003), Statistical analysis of relativistic electron energies for cyclotron resonance with EMIC waves observed on CRRES, *J. Geophys. Res.*, *108*, doi:10/1029/2002JA009700.

Meredith, N. P., R. B. Horne, R. M. Thorne, D. Summers, and R. R. Anderson (2004), Substorm dependence of plasmaspheric hiss, *J. Geophys. Res.*, *109*, A06209, doi: 10.1029/2004JA010387.

Meredith, N. P., R. B. Horne, S. A. Glauert, and R. R. Anderson (2007), Slot region electron loss timescales due to plasmaspheric hiss and lightning-generated whistlers, *J. Geophys. Res.*, *112*, A08214, doi:10.1029/2007JA012413.

Meredith, N. P., R. B. Horne, T. Kersten, B. J. Fraser, and R. S. Grew (2014), Global morphology and spectral properties of EMIC waves derived from CRRES observations, *J. Geophys. Res.*, *119*, 5328, doi:10.1002/2014JA020064.

Millan, R. M., and R. M. Thorne (2007), Review of radiation belt relativistic electron losses, *J. Atmos. Solar-Terr. Phys.*, *69*, 362, doi:10.1029/2004BK000104.

Millan, R. M., R. P. Lin, D. M. Smith, K. R. Lorentzen, and M. P. McCarthy (2002), X-ray observations of MeV electron precipitation with a balloon-borne germanium spectrometer, *Geophys. Res. Lett.*, *29*, 2194, doi:10.1029/2002GL015922.

Millan, R. M., R. P. Lin, D. M. Smith, and M. P. McCarthy (2007), Observation of relativistic electron precipitation during a rapid decrease of trapped relativistic electron flux, *Geophys. Res. Lett.*, *34*, L10101, doi:10.1029/2006GL028653.

Mosier, S. R., M. L. Kaiser, and L. W. Brown (1973), Observations of noise bands asociated with the upper hybrid resonance by the IMP 6 radio astronomy experiment, *J. Geophys. Res.*, *78*, 1673.

Ni, B., J. Bortnik, R. M. Thorne, Q. Ma, and L. Chen (2013), Resonant scattering and resultant pitch angle evolution of relativistic electrons by plasmaspheric hiss, *J. Geophys. Res.*, *118*, 7740, doi:10.1002/2013JA019260.

O'Brien, T. P., K. R. Lorentzen, I. R. Mann, N. P. Meredith, J. B. Blake, J. F. Fennell, M. D. Looper, D. K. Milling, and R. R. Anderson (2003), Energization of relativistic electrons in the presence of ULF power and MeV microbursts: Evidence for dual ULF and VLF acceleration, *J. Geophys. Res.*, *108*(A8), 1329, doi:10.1029/2003JA009784.

Ogilvie, K. W., et al. (1995), SWE, a comprehensive plasma instrument for the wind spacecraft, *Space Sci. Rev.*, *71*, 55.

Olsen, R. C., S. D. Shawhan, D. L. Gallagher, C. R. Chappell, and J. L. Green (1987), Plasma observations at the earth's magnetic equator, *J. Geophys. Res.*, *92*, 2385, doi:

10.1029/JA092iA03p02385.

Olson, W. P., and K. A. Pfitzer (1977), Magnetospheric magnetic field modeling, *Tech. rep.*

Reeves, G. D. (2007), Radiation Belt Storm Probes: A New Mission for Space Weather Forecasting, *Space Weather*, *5*, S11002, doi:10.1002/2007SW000341.

Reeves, G. D., et al. (2016), Energy-dependent dynamics of kev to mev electrons in the inner zone, outer zone, and slot regions, *J. Geophys. Res.*, *121*, doi:10.1002/2015JA021569.

Rodger, C. J., A. T. Hendry, M. A. Clilverd, C. A. Kletzing, J. B. Brundell, and G. D. Reeves (2015), High-resolution in situ observations of electron precipitation-causing emic waves, *Geophys. Res. Lett.*, *42*, 9633, doi:10.1002/2015GL066581.

Sazhin, S. S., and M. Hayakawa (1992), Magnetospheric chorus emissions: A review, *Planet. Space Sci.*, *40*, 681–697.

Shprits, Y. Y., R. M. Thorne, R. Friedel, G. D. Reeves, J. F. Fennell, D. Baker, and S. G. Kanekal (2006), Outward radial diffusion driven by losses at magnetopause, *J. Geophys. Res.*, p. submitted.

Shprits, Y. Y., N. P. Meredith, and R. M. Thorne (2007), Parameterization of radiation belt electron loss timescales due to interactions with chorus waves, *Geophys. Res. Lett.*, *34*, L11110, doi:10.1029/2006GL029050.

Shue, J.-H., J. K. Chao, H. C. Fu, C. T. Russell, P. Song, K. K. Khurana, and H. J. Singer (1997), A new functional form to study the solar wind control of the magnetopause size and shape, *J. Geophys. Res.*, *102*, 9497, doi:10.1029/97JA00196.

Spasojevic, M., Y. Y. Shprits, and K. Orlova (2015), Global empirical models of plasmaspheric hiss using Van Allen Probes, *J. Geophys. Res.*, *120*, 10, doi:

10.1002/2015JA021803.

Stone, E. C., A. M. Frandsen, R. A. Mewaldt, E. R. Christian, D. Margolies, J. F. Ormes, and F. Snow (1998), The Advanced Composition Explorer, *Space Sci. Rev.*, *86*, 1, doi: 10.1023/A:1005082526237.

Summers, D., and R. M. Thorne (2003), Relativistic electron pitch-angle scattering by electromagnetic ion cyclotron waves during geomagnetic storms, *J. Geophys. Res.*, *108*(A4), 1143, doi:10.1029/2002JA009489.

Summers, D., B. Ni, and N. P. Meredith (2007), Timescales for radiation belt electron acceleration and loss due to resonant wave-particle interactions: 2. Evaluation for VLF chorus, ELF hiss, and electromagnetic ion cyclotron waves, *J. Geophys. Res.*, *112*, A04207, doi:10.1029/2006JA011993.

Summers, D., Y. Omura, S. Nakamura, and C. A. Kletzing (2014), Fine structure of plasmaspheric hiss, *J. Geophys. Res.*, *119*, 9134, doi:10.1002/2014JA020437.

Thorne, R. M., and C. F. Kennel (1971), Relativistic electron precipitation during magnetic storm main phase, *J. Geophys. Res.*, *76*, 4446.

Thorne, R. M., E. J. Smith, R. K. Burton, and R. E. Holzer (1973), Plasmaspheric hiss, *J. Geophys. Res.*, *78*, 1581, doi:10.1029/JA078i010p01581.

Turner, D. L., et al. (2014a), On the cause and extent of outer radiation belt losses during the 30 September 2012 dropout event, *J. Geophys. Res.*, *119*, 1530, doi: 10.1002/2013JA019446.

Turner, D. L., et al. (2014b), Competing source and loss mechanisms due to wave-particle interactions in Earth's outer radiation belt during the 30 September to 3 October 2012 geomagnetic storm, *J. Geophys. Res.*, *119*, 1960, doi:10.1002/2014JA019770.

Ukhorskiy, A. Y., M. I. Sitnov, R. M. Millan, B. T. Kress, J. F. Fennell, S. G. Claudepierre, and R. J. Barnes (2015), Global storm time depletion of the outer electron belt, *J. Geophys. Res.*, *120*, 2543, doi:10.1002/2014JA020645.

Usanova, M. E., et al. (2014), Effect of EMIC waves on relativistic and ultrarelativistic electron populations: Ground-based and Van Allen Probes observations, *Geophys. Res. Lett.*, *41*, 1375, doi:10.1002/2013GL059024.

Van Allen, J. A., and L. A. Frank (1959), Radiation around the Earth to a radial distance of 107,400 km, *Nature*, *183*, 430.

Wang, D., et al. (2015), Statistical characteristics of EMIC waves: Van Allen Probe observations, *J. Geophys. Res.*, *120*, 4400, doi:10.1002/2015JA021089.

Woodger, L. A. (2012), Investigating EMIC waves as a precipitation mechanism for relativistic electrons, Ph.D. thesis, Dartmouth College, Hanover, NH.

Woodger, L. A., A. J. Halford, R. M. Millan, M. P. McCarthy, D. M. Smith, G. S. Bowers, J. G. Sample, B. R. Anderson, and X. Liang (2015), A summary of the BARREL campaigns: Technique for studying electron precipitation, *J. Geophys. Res.*, *120*, 4922, doi:10.1002/2014JA020874.

Yu, J., L. Y. Li, J. B. Cao, Z. G. Yuan, G. D. Reeves, D. N. Baker, J. B. Blake, and H. Spence (2015a), Multiple loss processes of relativistic electrons outside the heart of outer radiation belt during a storm sudden commencement, *J. Geophys. Res.*, *120*, 10, doi:10.1002/2015JA021460.

Yu, X., et al. (2015b), In situ observations of EMIC waves in O^+ band by the Van Allen Probe A, *Geophys. Res. Lett.*, *42*, 1312, doi:10.1002/2015GL063250.

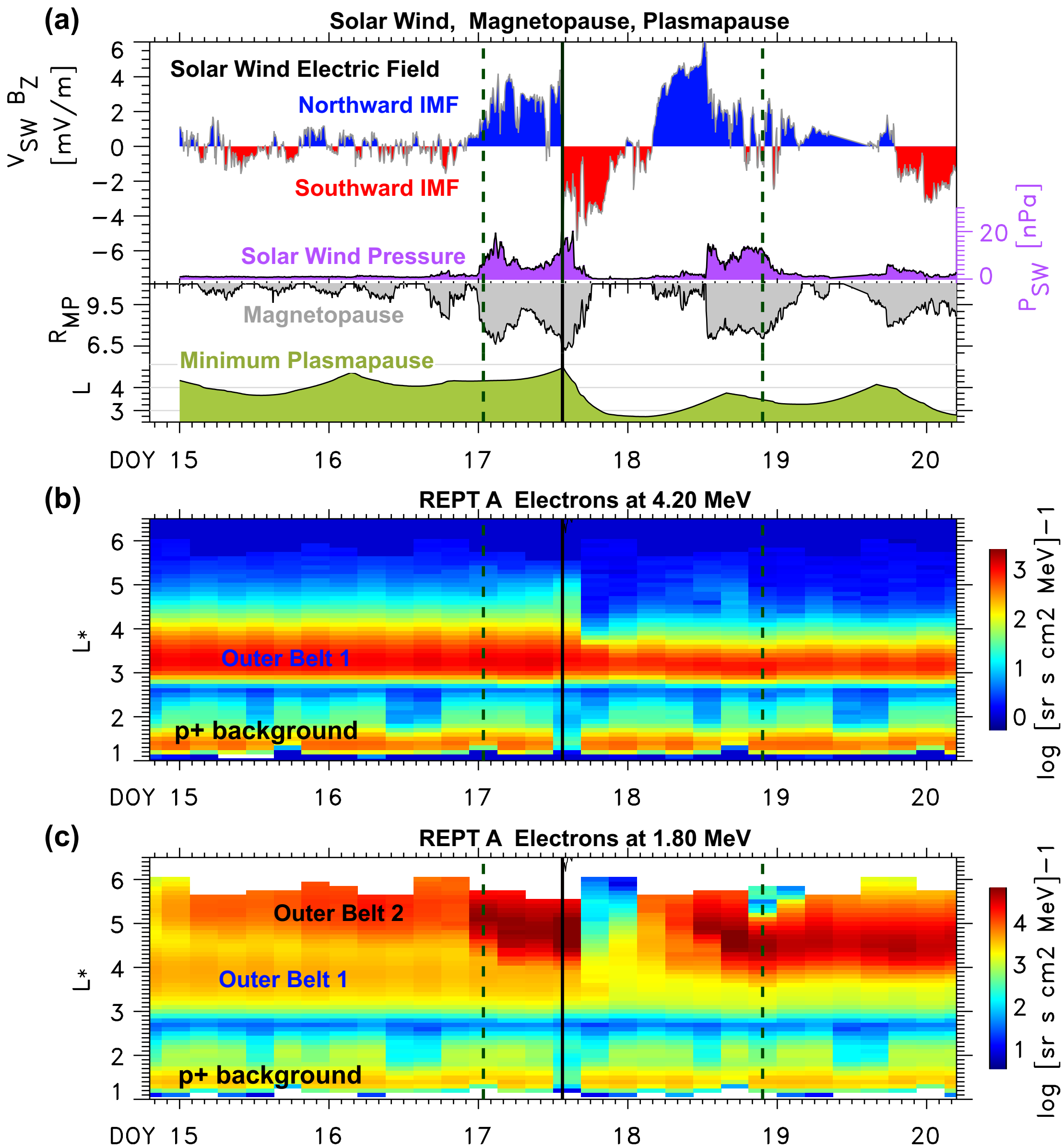

Figure 1. Overview of the 15–20 January 2013 disturbance event [*Goldstein et al.*, 2014b], initiated on 1330 UT on 17 January (solid vertical line). Dashed vertical lines are times used for peak-finding examples, Figure 2. **(a)** OMNI solar wind electric field (E_{SW}) and pressure (P_{SW}), subsolar magnetopause (R_{MP}) using *Shue et al.* [1997], and minimum test-particle-simulated plasmapause (cf. Section 4). **(b,c)** REPT 4.20 MeV and 1.80 MeV electrons from Van Allen Probes A.

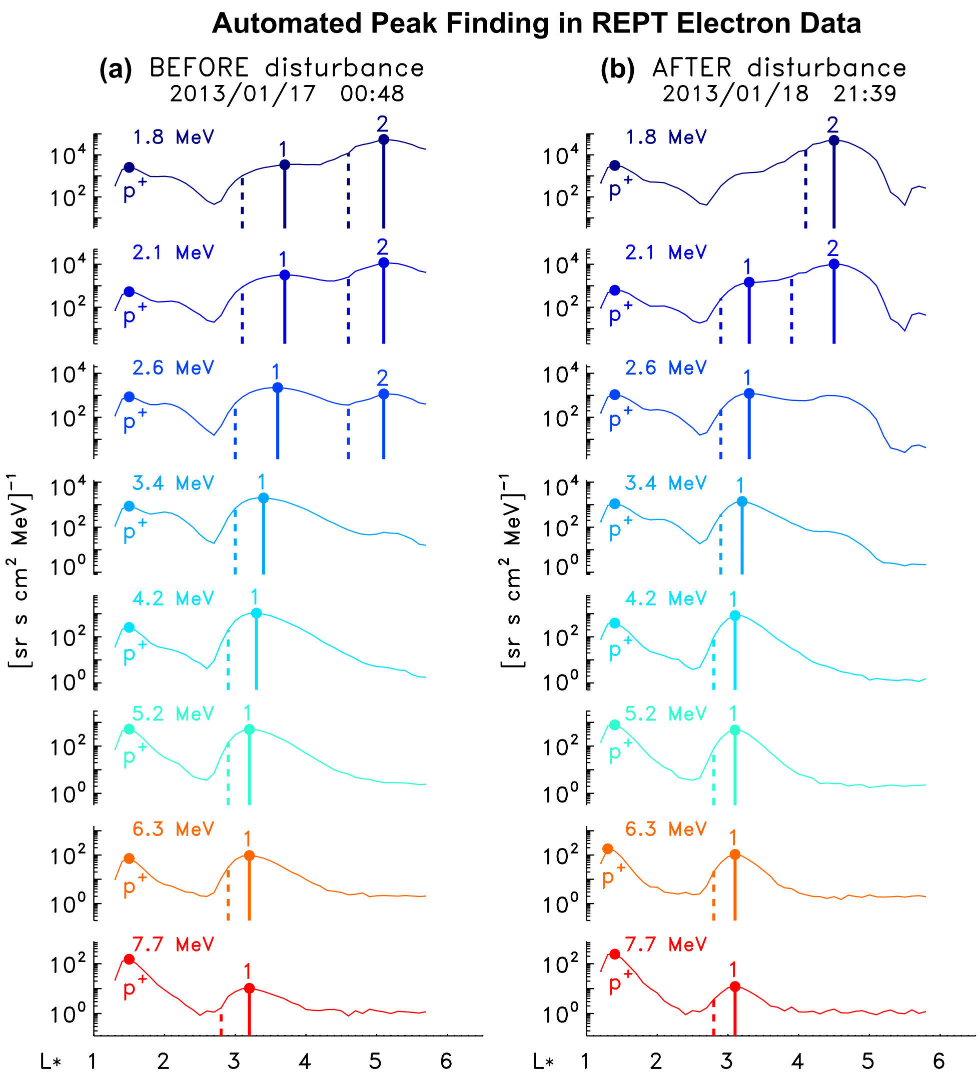

Figure 2. Electron peak and edge finder, applied to REPT A data for two selected times and 8 energies. Peaks of outer belts 1 and 2: numbered ("1" or "2") dots and vertical lines. Corresponding exp(−1) edges: dashed lines. Points labeled "p^+" are proton contamination.

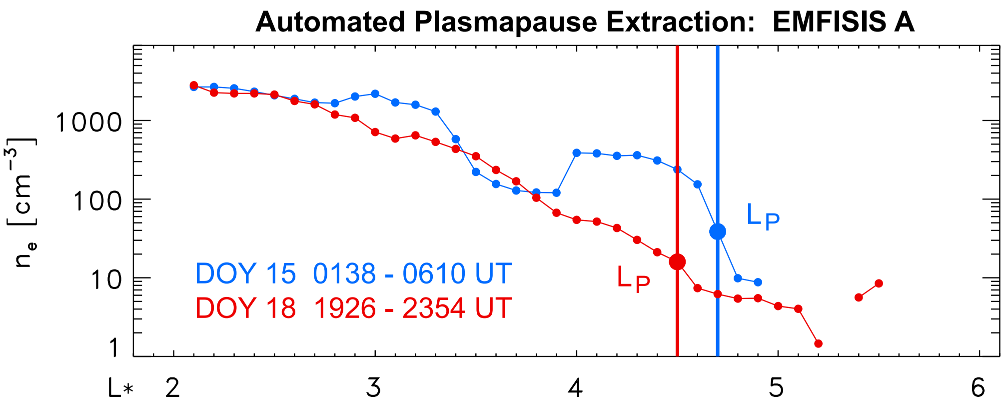

Figure 3. Plasmapause finder, applied to EMFISIS A data (binned in L^* to match REPT A data from Figure 2) for two selected times.

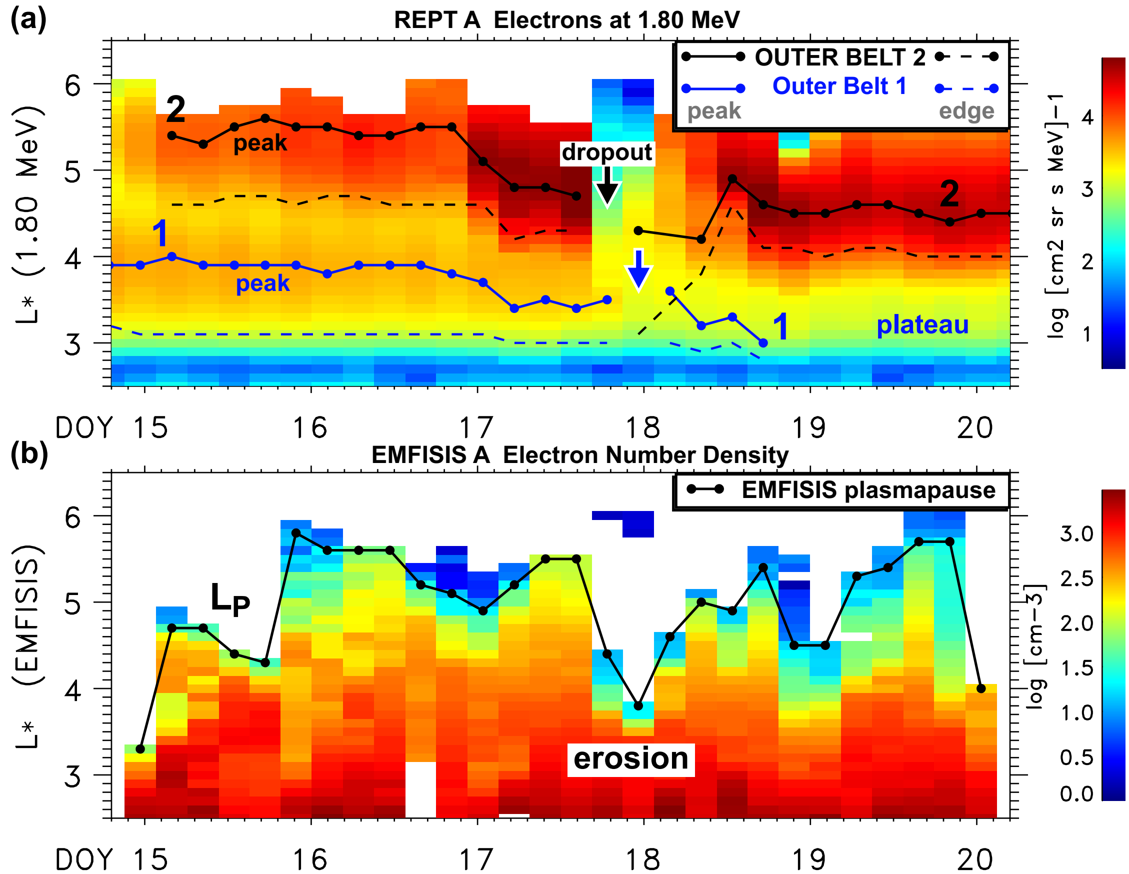

Figure 4. Automated extraction of outer belt and plasmapause locations for 15–20 January 2013. **(a)** 1.8 MeV REPT A spectrogram with extracted peaks (f_{peak}, solid lines) and edges (f_{edge}, dashed lines). Two outer belts ('1' and '2') are found. **(b)** EMFISIS A densities binned to match REPT spectrogram; the black line is the extracted plasmapause (L_{P}).

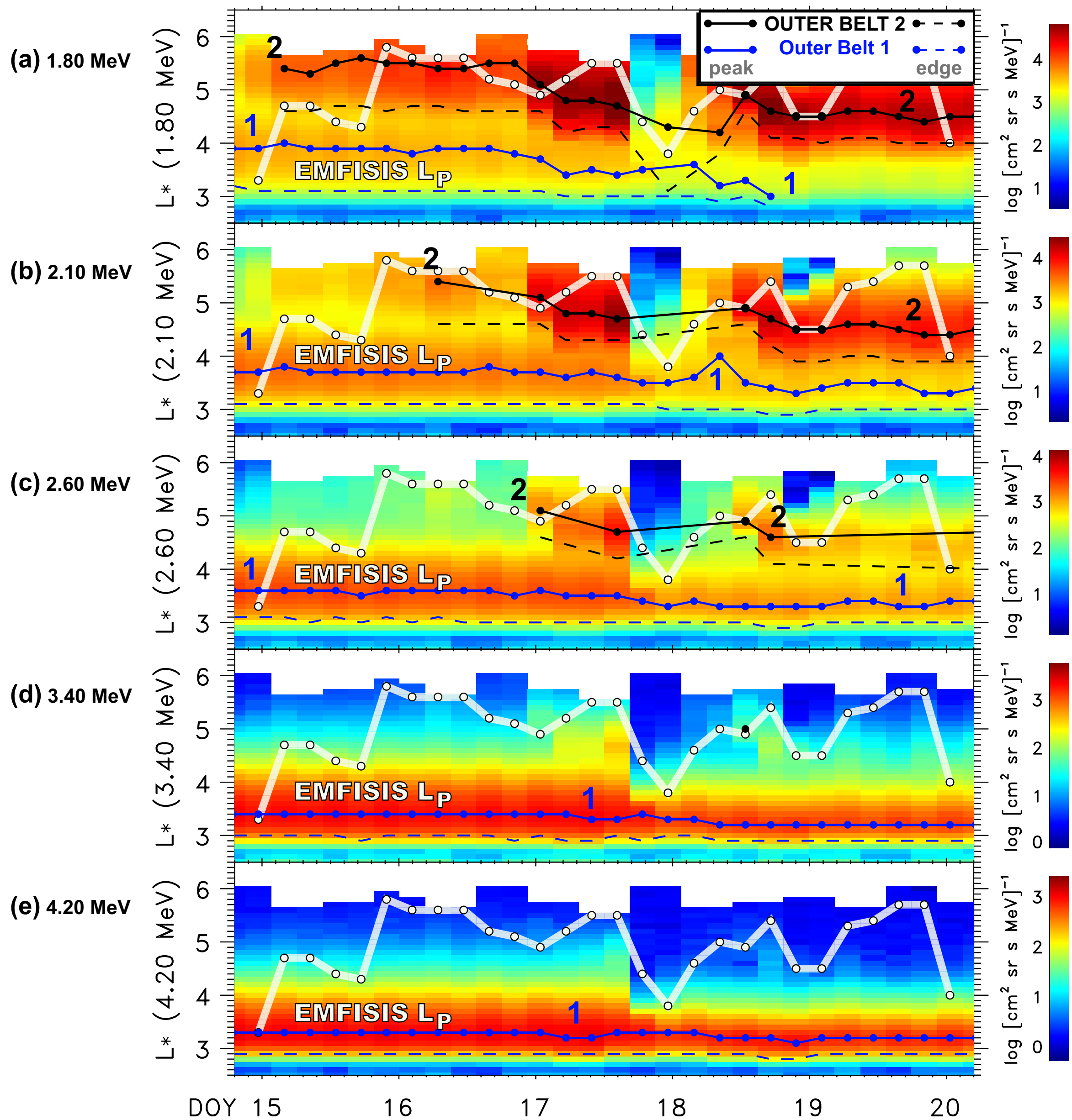

Figure 5. Comparison of outer belts and plasmapause, 15–20 January 2013. Each panel shows REPT A spectrogram with outer belt peaks and edges as in Figure 4a. The plasmapause (L_P) is overplotted in white. Five energies are shown: **(a)** 1.8 MeV, **(b)** 2.1 MeV, **(c)** 2.6 MeV, **(d)** 3.4 MeV, **(e)** 4.2 MeV.

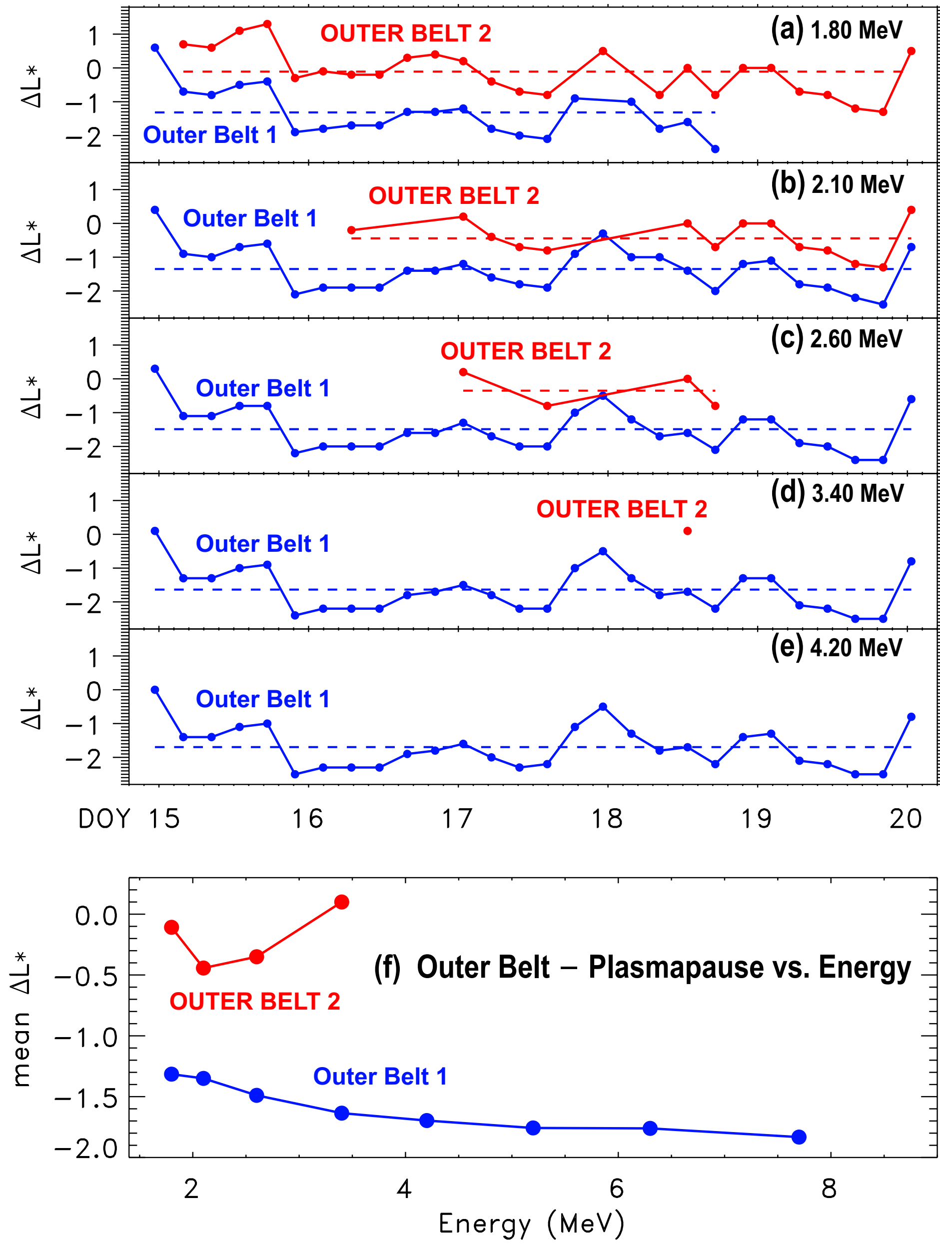

Figure 6. Difference between the outer belts and plasmapause. The blue and red curves are for outer belts 1 and 2, respectively. Dashed lines give the per-energy mean values ($\langle \Delta L^* \rangle$) for 15–18. Five energies are shown: **(a)** 1.8 MeV, **(b)** 2.1 MeV, **(c)** 2.6 MeV, **(d)** 3.4 MeV, **(e)** 4.2 MeV. **(f)** Mean difference $\langle \Delta L^* \rangle$ versus energy.

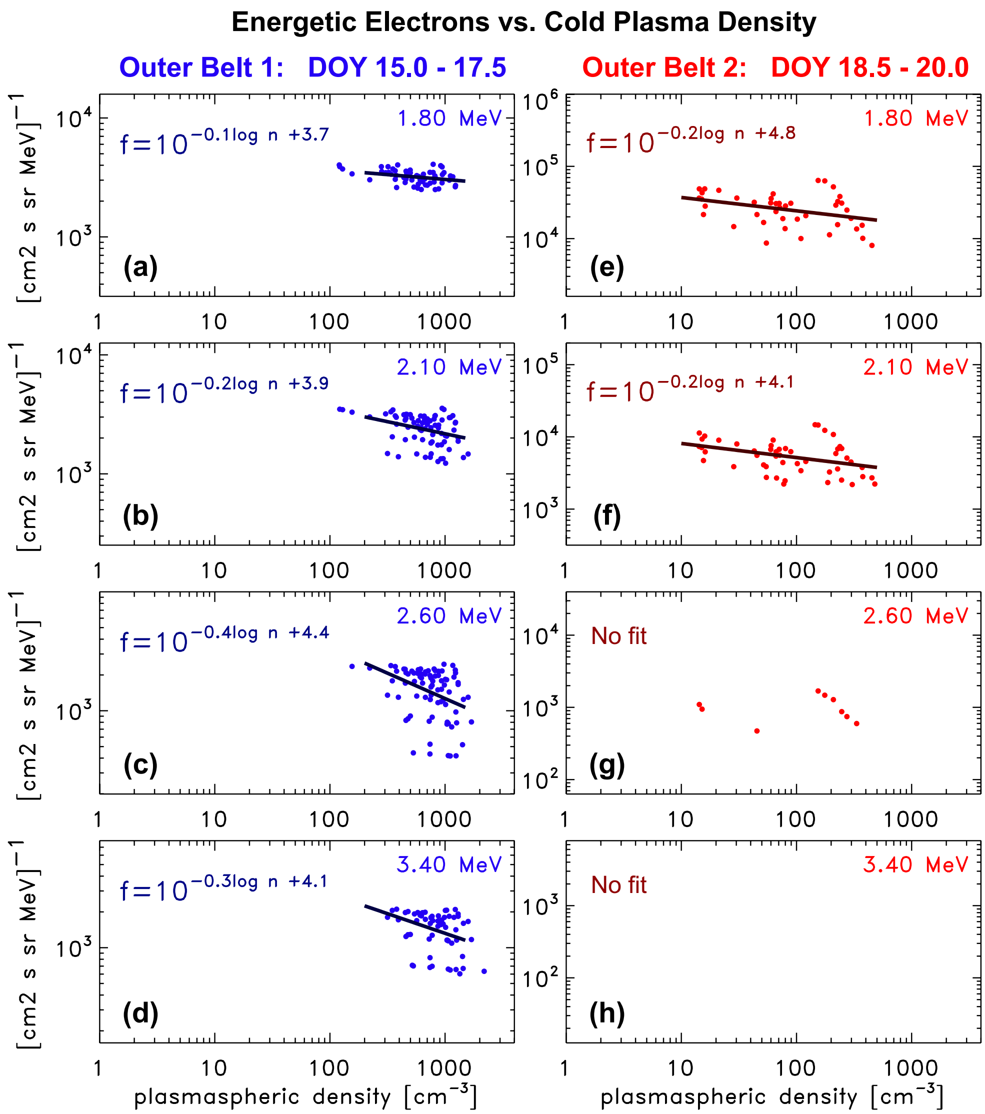

Figure 7. Relativistic electron flux (f) versus cold plasma density (n) at four selected energies during steady conditions. Blue (red) data are for outer belt 1 (2), from the region earthward of the peak (cf. text). The thick lines are linear fits to $\log f$ versus $\log n$.

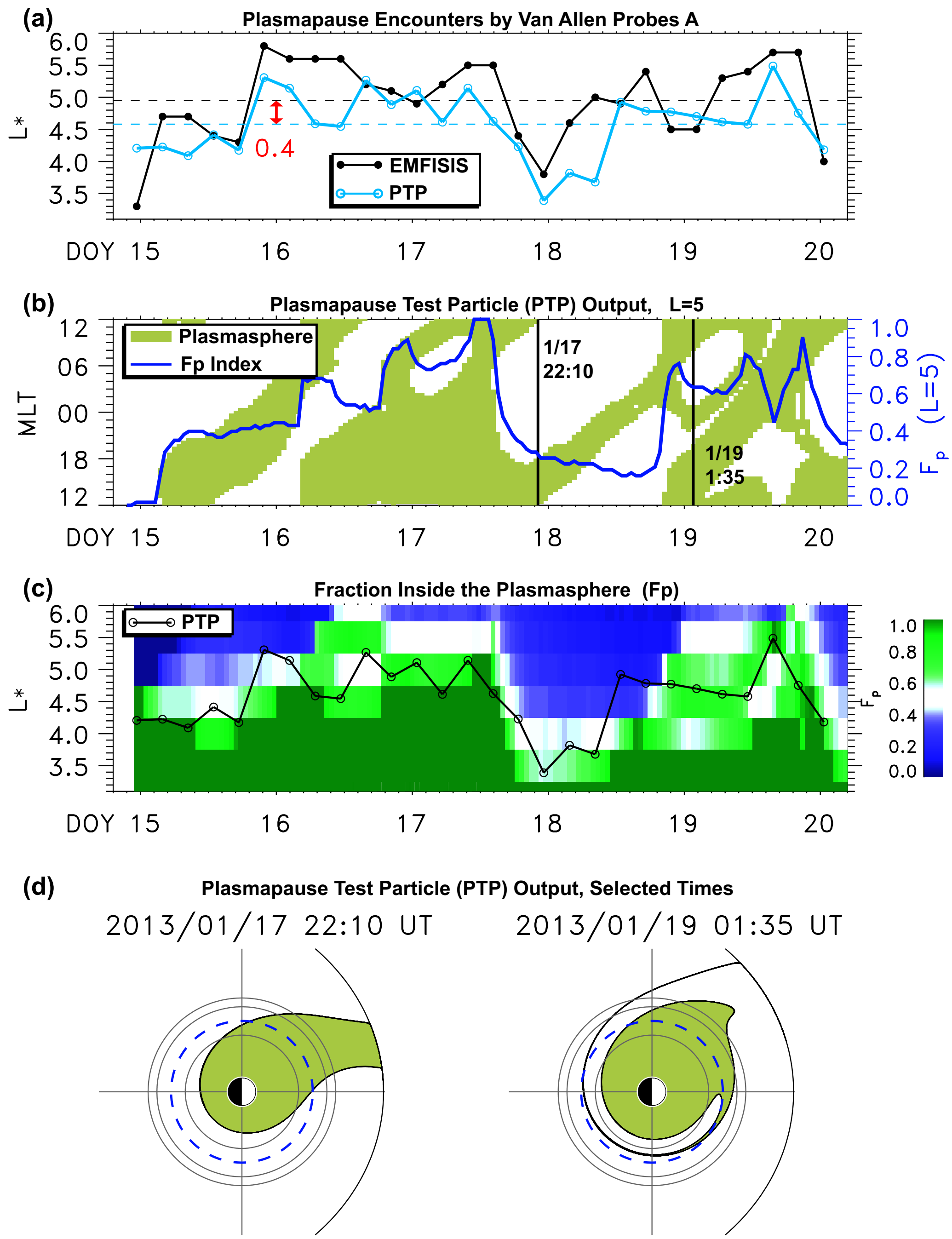

Figure 8. Plasmapause test particle (PTP) simulation results for global context. **(a)** Plasmapause encounters by actual and virtual Van Allen Probes A spacecraft. **(b)** Cold plasma regions (green) versus MLT and time, at $L = 5$. Blue curve is F_p, the fraction of drift orbit inside the plasmasphere (cf. text). **(c)** 2D plot of F_p versus L^* and time; black curve is PTP plasmapause. **(d)** Equatorial plasmapause at two selected times. The Sun is to the right. Black circles at $L = [4, 6, 6.6]$; blue dashed circle at $L = 5$.

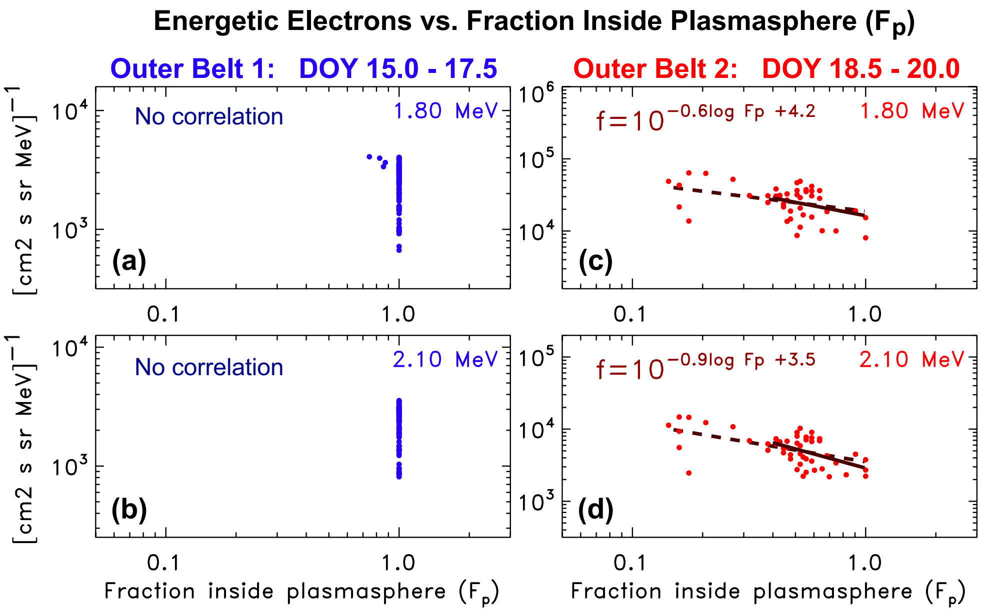

Figure 9. Relativistic electron flux (f) versus fraction of drift orbit inside the plasmasphere (F_p) at two selected energies during steady conditions. Blue (red) data are for outer belt 1 (2), from the region earthward of the peak. The thick lines are linear fits to $\log f$ versus $\log F_p$. The dashed lines are alternate fits for a wider range of F_p (cf. text).

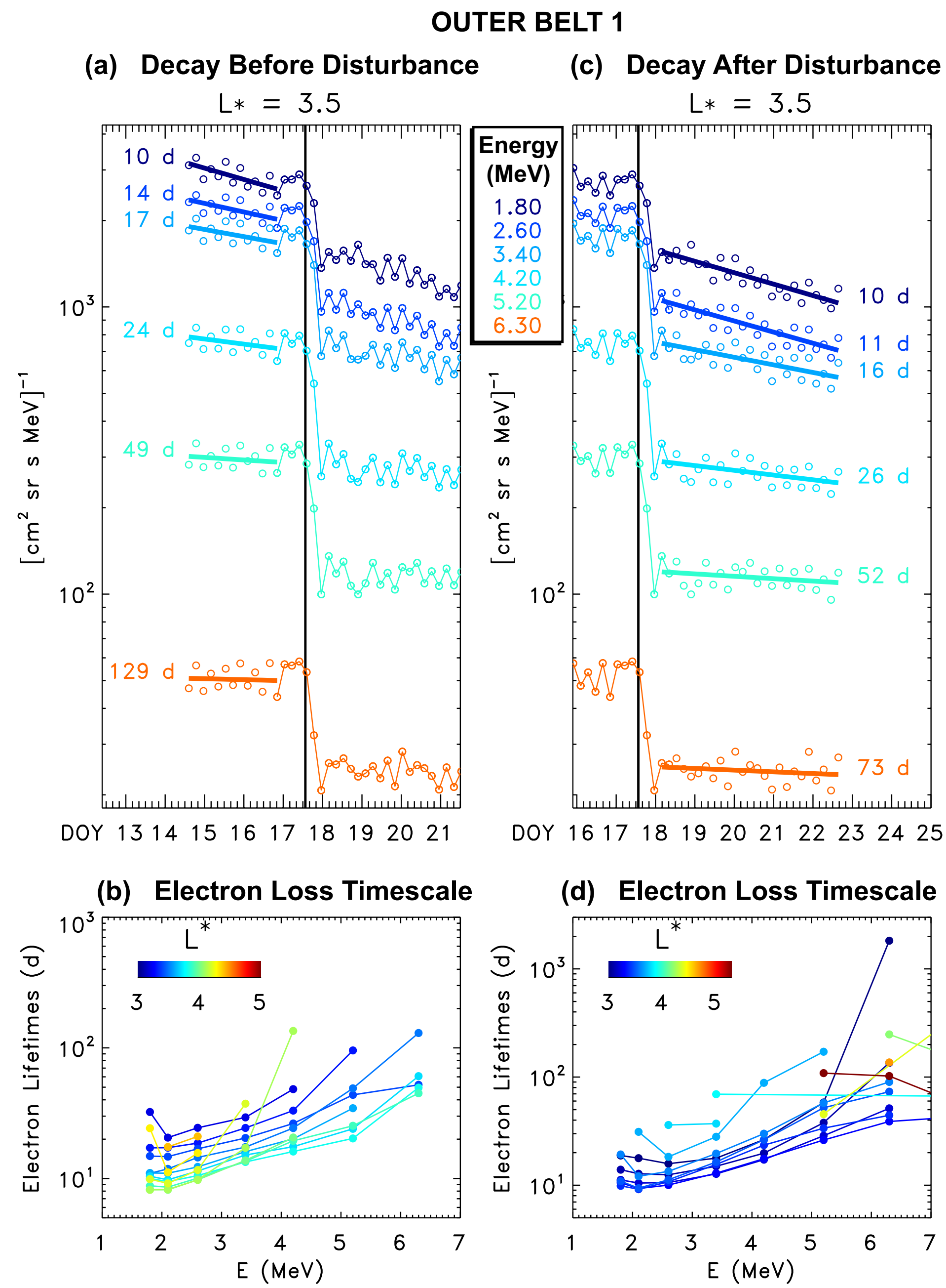

Figure 10. Outer belt 1 ($L^* = 3.5$) loss before and after the disturbance (vertical black line). **(a,c)** Belt 1 electron flux versus time for energies spanning 1.8–6.3 MeV. Thick lines are exponential ($\exp(-t/\tau)$) fits to log flux before day 17 and after day 18. Loss timescales between 10 d at 1.8 MeV and 129 d at 6.3 MeV are consistent with plasmaspheric hiss. **(b, d)** Outer belt 1, pre- and post-disturbance loss timescale (τ) versus energy and L^*.

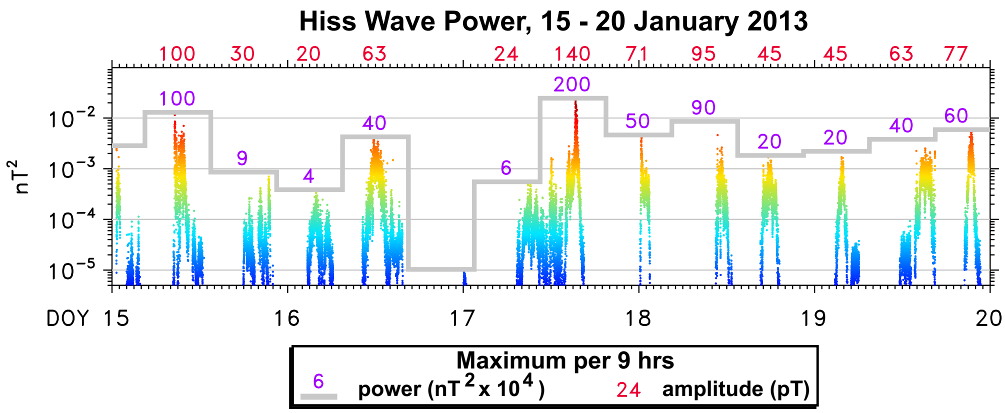

Figure 11. Estimate of hiss wave power for 15-20 January 2013 (cf. Appendix A2). The thick gray line indicates the peak value per 9-h interval; purple number labels indicate power levels (in $nT^2 \times 10^4$), rounded to one significant digit. The red numbers at the top of the plot indicate the corresponding hiss amplitudes (in pT). Points are color-coded by power to emphasize peak values.

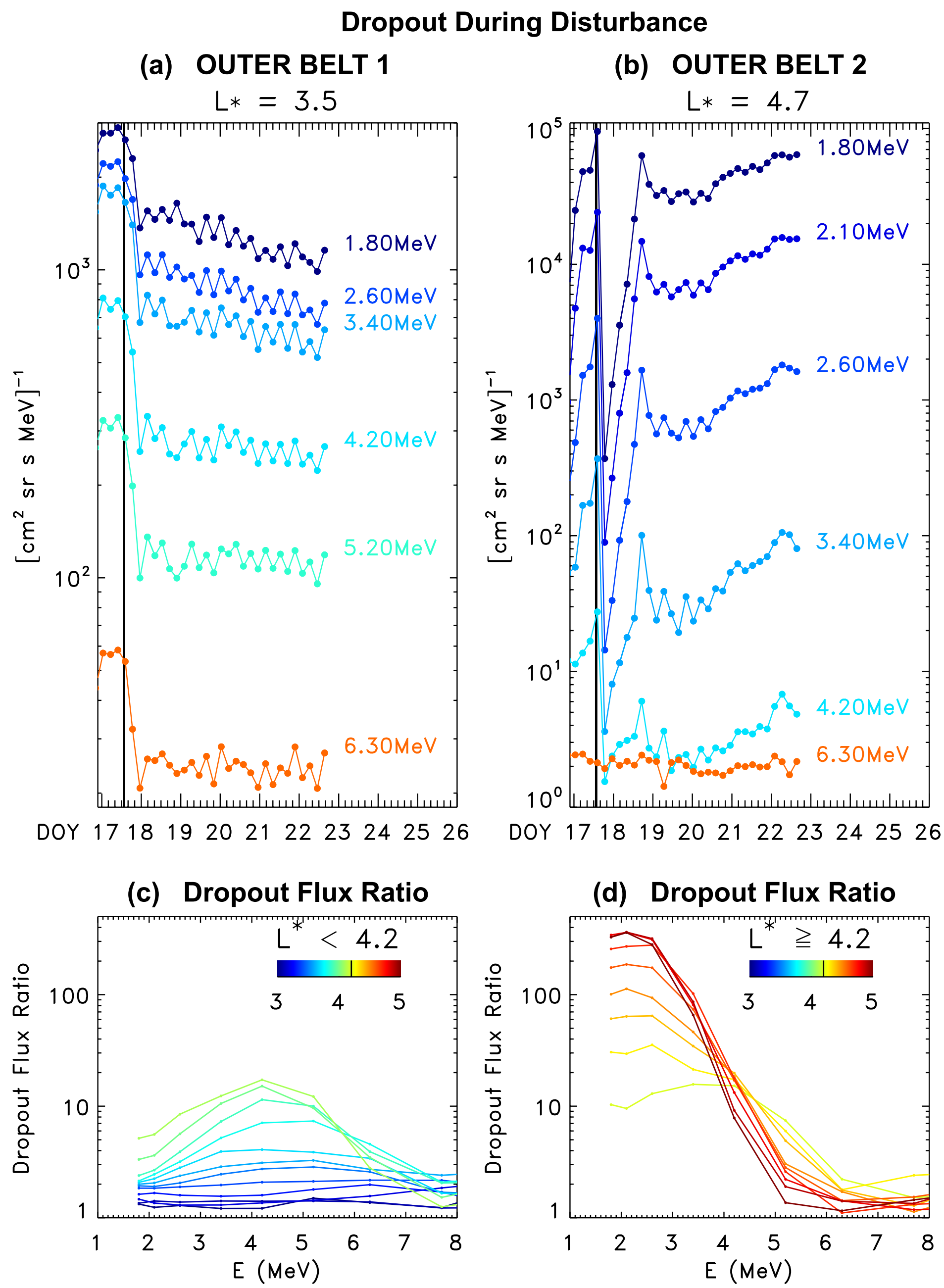

Figure 12. Flux dropouts during the disturbance (vertical black line). **(a)** Outer belt 1 ($L^* = 3.5$) electron flux versus time for energies spanning 1.8–6.3 MeV shows modest (factor of 2–4) drop with no post-disturbance recovery. **(b)** Outer belt 2 ($L^* = 4.7$) electron flux shows post-disturbance dropouts of up to two orders of magnitude (decreasing with energy). Post-disturbance fluxes recovered in <2 days. **(c, d)** Dropout flux ratio (cf. text) versus energy and L^*, with larger dropouts at higher L^*.

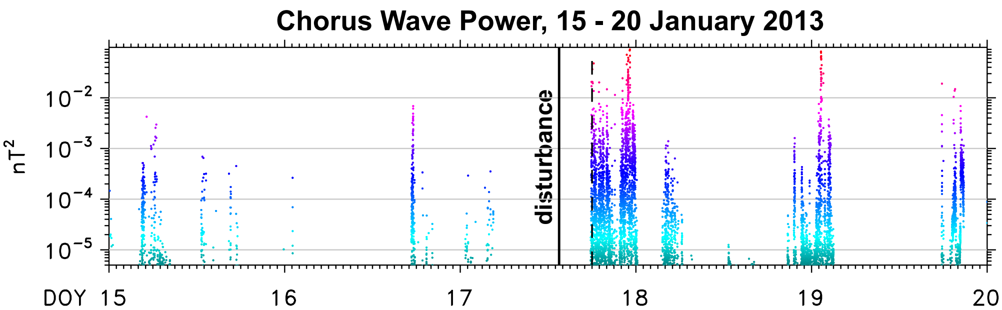

Figure 13. Estimate of chorus wave power for 15-20 January 2013 (cf. Appendix A3). Points are color-coded by power to emphasize peak values.

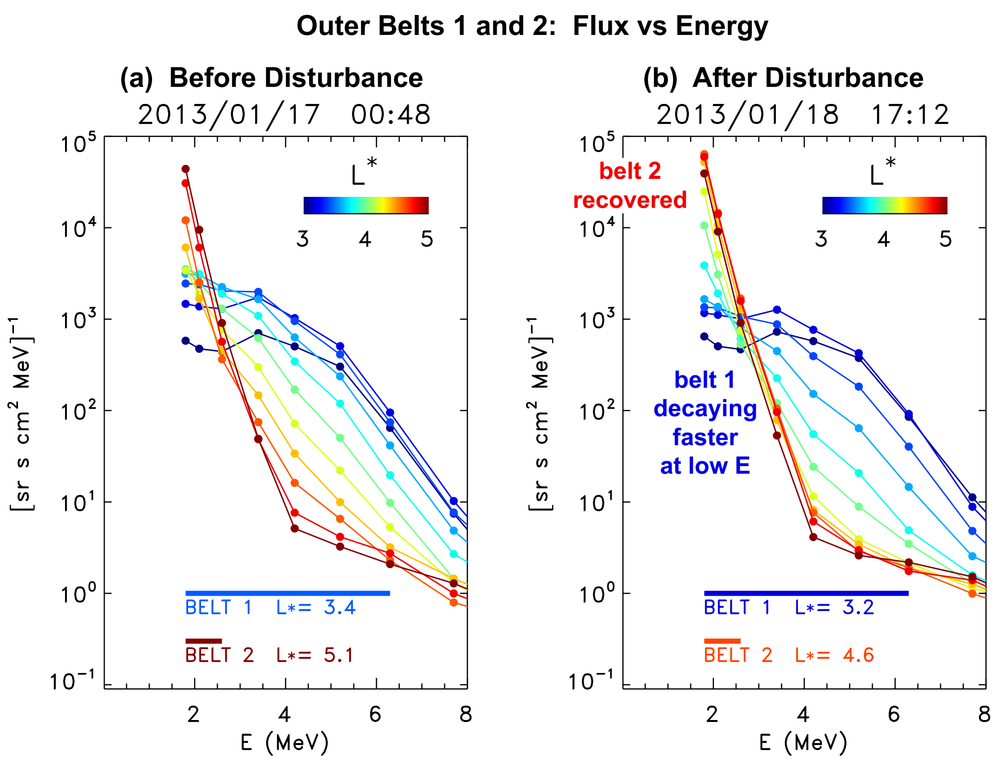

Figure 14. Relativistic electron flux versus energy and location, **(a)** before and **(b)** after the disturbance at 1330 UT on 17 January. Color indicates L^*. Horizontal bars at the bottom of each plot indicate the energy extent of belts 1 and 2 (i.e., the energy range of extracted peaks, as in Figure 5). The energy-averaged peak locations (L_{peak}) are also indicated.

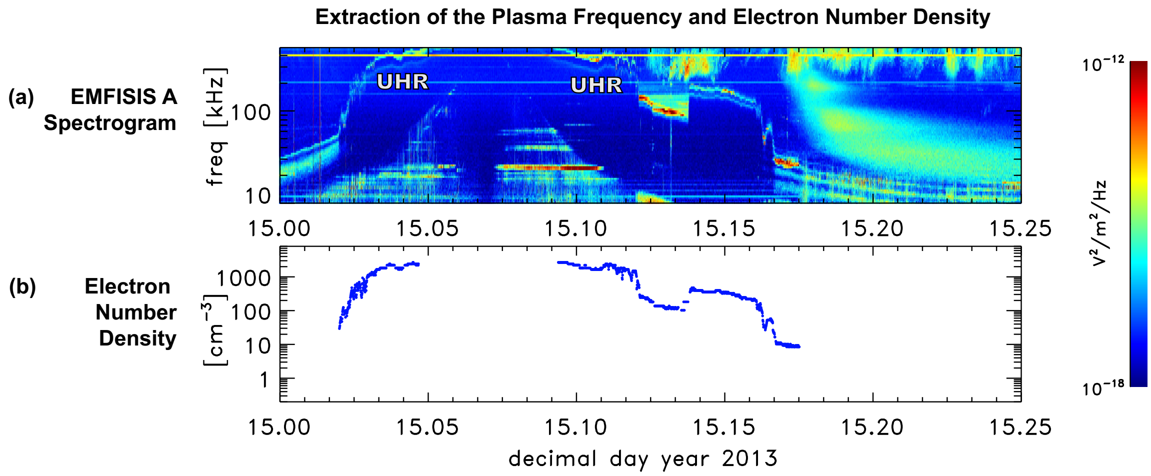

Figure A.1. Analysis of EMFISIS HFR wave data. **(a)** EMFISIS A HFR spectrogram showing UHR line (cf. text). **(b)** Extracted electron number density n_e.

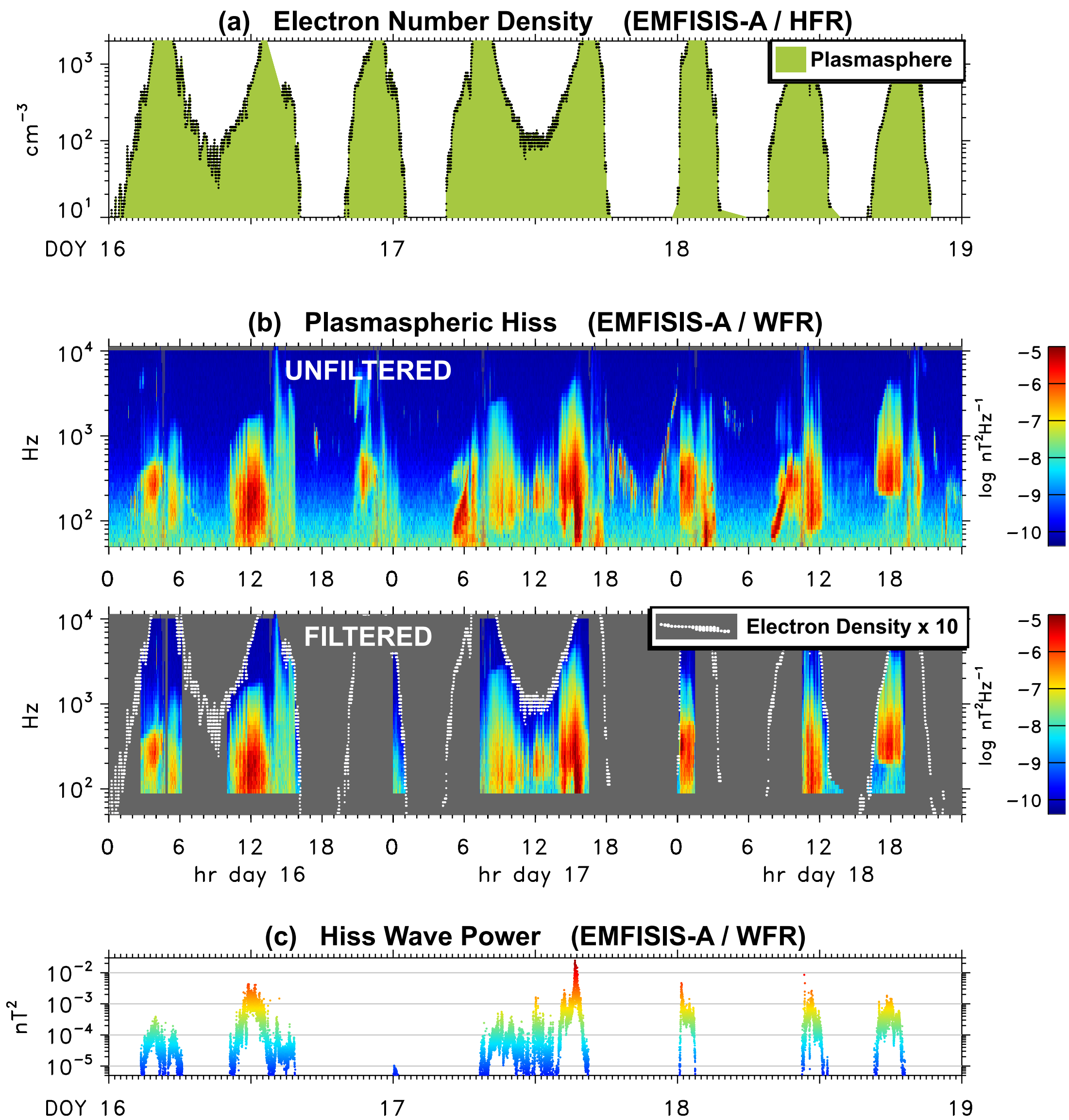

Figure A.2. Analysis of EMFISIS WFR wave data to identify plasmaspheric hiss. **(a)** Electron number density derived as in Figure A.1. **(b)** EMFISIS A WFR spectrograms, unfiltered and filtered to isolate hiss (cf. text). **(c)** Hiss wave power.

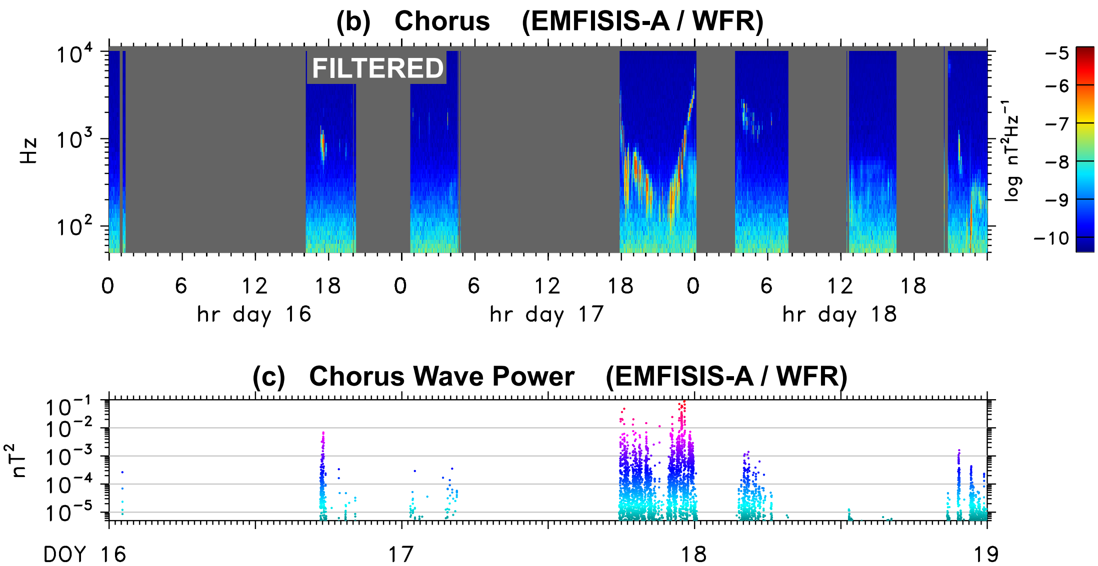

Figure A.3. Analysis of EMFISIS WFR wave data to identify chorus. **(a)** EMFISIS A WFR spectrograms, filtered to isolate chorus (cf. text). **(b)** Chorus wave power.